J. Fluid Mech. (2015), *vol.* 764, *pp.* 362–394. © Cambridge University Press 2015
doi:10.1017/jfm.2014.715

Direct numerical simulation of a turbulent jet impinging on a heated wall

T. Dairay[1],†, **V. Fortuné**[2], **E. Lamballais**[2] **and L.-E. Brizzi**[2]

[1]Turbulence, Mixing and Flow Control Group, Department of Aeronautics, Imperial College London, London SW7 2AZ, UK

[2]Institute PPRIME, Department of Fluid Flow, Heat Transfer and Combustion, CNRS – Université de Poitiers ENSMA, Téléport 2, Boulevard Marie et Pierre Curie, BP 30179, 86962 Futuroscope Chasseneuil CEDEX, France

(Received 6 June 2014; revised 3 November 2014; accepted 5 December 2014; first published online 5 January 2015)

Direct numerical simulation (DNS) of an impinging jet flow with a nozzle-to-plate distance of two jet diameters and a Reynolds number of 10 000 is carried out at high spatial resolution using high-order numerical methods. The flow configuration is designed to enable the development of a fully turbulent regime with the appearance of a well-marked secondary maximum in the radial distribution of the mean heat transfer. The velocity and temperature statistics are validated with documented experiments. The DNS database is then analysed focusing on the role of unsteady processes to explain the spatial distribution of the heat transfer coefficient at the wall. A phenomenological scenario is proposed on the basis of instantaneous flow visualisations in order to explain the non-monotonic radial evolution of the Nusselt number in the stagnation region. This scenario is then assessed by analysing the wall temperature and the wall shear stress distributions and also through the use of conditional averaging of velocity and temperature fields. On one hand, the heat transfer is primarily driven by the large-scale toroidal primary and secondary vortices emitted periodically. On the other hand, these vortices are subjected to azimuthal distortions associated with the production of radially elongated structures at small scale. These distortions are responsible for the appearance of very high heat transfer zones organised as cold fluid spots on the heated wall. These cold spots are shaped by the radial structures through a filament propagation of the heat transfer. The analysis of probability density functions shows that these strong events are highly intermittent in time and space while contributing essentially to the secondary peak observed in the radial evolution of the Nusselt number.

Key words: jets, turbulence simulation, vortex dynamics

1. Introduction

Due to its industrial importance, impinging jet flow has received considerable attention, with particular interest in the modification of heat transfer at the wall. In practical applications, impinging jets are efficient tools in cooling or heating systems

---

† Email address for correspondence: tdairay@hotmail.fr

through their ability to enhance heat transfer between the fluid and the impinged solid target. The cooling of aircraft engines is an example where impinging jets are used to enhance the heat transfer. Temperature control of the turbine is one of the major limiting factors affecting engine performance. The lifetime of the blades is in practice directly related to the cooling effectiveness. Even a small improvement of this effectiveness can lead to significant benefits. For the case of a turbine blade, Yeh & Stepka (1984) found that an uncertainty of ±10 % in the heat transfer coefficient may lead to an uncertainty of ±15 °C in the wall temperature. This could be seen as a small difference in temperature. However, Dailey (2000) has shown that an error of 15 °C in the estimated temperature of a turbine blade can shorten its life by a factor of two. The resulting industrial cost explains why it is worth developing very accurate tools for heat transfer prediction through the development of new models guided by a better knowledge of the involved physical processes.

Although it is widely documented in the literature, impinging jet flow is not sufficiently well known to make it possible to understand or even to predict the influence of various parameters such as jet type (laminar/turbulent regime), impingement distance, confinement, the Reynolds and Mach numbers, plate heating, temperature difference, etc. This lack of knowledge inhibits efficient optimisation of industrial systems where thermal control is expected with the help of impinging jets. The main difficulty in analysing these different effects is that they are the consequence of subtle physical processes involving space and time scales that are not easily measurable experimentally. This point has been shown in some recent studies with the joint development of measurement techniques like particle image velocimetry (PIV) (see El Hassan *et al.* 2012), time-resolved tomographic PIV (TR-TOMO PIV) (see Violato *et al.* 2012) and numerical methods, especially using direct numerical simulation (DNS) and large eddy simulation (LES) (see Dewan, Dutta & Srinivasan 2012; Wilke & Sesterhenn 2015). Despite the wide range of physical scales considered in these studies, the understanding of heat transfer on the impingement plate is still a disputed question, especially when the jet is fully turbulent, i.e. for a realistic regime for industrial applications.

1.1. *Vortical structures of the impinging jet flow*

The first impinging jet flow experiments are summarised in the review of Gauntner, Livingood & Hrycak (1970). These experiments are mainly focused on basic turbulent statistics allowing the identification of characteristic flow regions and regimes. The impinging jet flow is commonly divided into three regions (see also Deshpande & Vaishnav 1982; Miller 1995). First, the free jet region is defined as the region where the flow is not influenced by the impingement plate. In this zone, the velocity is mainly axial and constant on the jet centreline. Second, in the stagnation region, the flow is deflected from its axial direction to a radial one. Third, in the wall jet region, the velocity is mainly radial, with the formation of a boundary layer developing along the radial direction. The boundary layer velocity profile is shaped as for a wall jet flow (with a maximum velocity at an intermediate distance from the wall). With increasing radial distance, its thickness increases whereas its maximum velocity decreases.

The near-wall vortical structures of impinging jet flow have been extensively investigated experimentally (e.g. Martin 1977; Jambunathan *et al.* 1992; Webb & Ma 1995; Hall & Ewing 2006). Didden & Ho (1985) analyse the unsteady separation of the boundary layer induced by the jet impingement. Forcing the jet to its natural frequency, they highlight the periodical separation of the boundary layer. Their measurements show that the vortical structures issuing from the shear layer of the jet are convected radially in the near-wall flow. These structures are called the primary vortices. Closer to the wall, counter-rotating vortices convected in the radial direction can also be observed but their formation is downstream of the radial location where primary vortices are first detected. That is why these structures are referred to as secondary vortices. Didden & Ho (1985) explain the unsteady separation mechanism in the impinging jet flow using the viscous–inviscid interaction theory. Each primary vortex, located in the inviscid region of the flow, is responsible for an upward fluid motion just downstream of it. This fluid motion involves an unsteady adverse pressure gradient: the flow decelerates in the near-wall region and accelerates in the inviscid zone. This process leads to the formation of an unstable shear layer between the viscous and inviscid regions. The resulting shear-layer instability produces a counter-rotating vortex roll-up that is associated with an unsteady separation of the boundary layer. In this mechanism, the unsteady separation is driven by the inviscid flow fluctuations through the viscous near-wall region.

Over the last decade, some numerical studies have been carried out to better understand the vortical structures in the impinging jet flow (e.g. Beaubert & Viazzo 2003; Lodato, Vervisch & Domingo 2009). Tsubokura *et al.* (2003) perform LES and DNS of forced round and plane impinging jets (DNS at Reynolds number $Re = 2000$ and LES at $Re = 6000$). Their work is mainly devoted to comparing plane and round jets and their related vortical structures. In particular, their simulations detect near-wall secondary vortices. Focusing on large-scale dynamics, Hadziabdic & Hanjalic (2008) perform an LES study of a turbulent jet at $Re = 23\,000$ and a nozzle to plate distance of $H/D = 2$ where D is the jet diameter. They show that the vortex roll-up phenomenon along the impingement plate is the main event governing flow dynamics. The connection between the convection of the primary vortices, the formation of the counter-rotating secondary vortices and the unsteady separation phenomena is well recovered. However, in the LES study of Uddin, Neumann & Weigand (2013), no unsteady separation is found in unforced impinging jets at $Re = 13\,000$ and $Re = 23\,000$ with the same nozzle-to-plate distance. Only strong acceleration regions connected with the convected primary structures are observed and related to the heat transfer distribution. All these events (primary and secondary vortices, unsteady separation) obviously have a direct influence on the mean heat transfer distribution, as discussed in § 1.2.

1.2. *Heat transfer at the impingement wall*

The link between flow and heat transfer can be examined statistically through an analysis of the mean heat transfer distribution and the main velocity statistics of the flow. The mean heat transfer coefficient $\langle h\rangle$ on the impingement plate is defined by $\langle h\rangle(r) = \varphi_p/(\langle T_w\rangle(r) - T_j)$, where r is the radial distance from the jet axis, φ_p is the heat flux density, T_j is the jet temperature and $\langle T_w\rangle$ is the mean wall temperature. It is usually non-dimensionalised by introducing the mean Nusselt number

$$\langle Nu\rangle\,(r) = \frac{\langle h\rangle\,(r)D}{\lambda}, \tag{1.1}$$

where λ is the thermal conductivity.

Gardon & Akfirat (1965) show that the heat transfer coefficient increases with the Reynolds number of the flow while keeping qualitatively a similar shape for each case. In particular, two local maxima are observed in the radial evolution of the mean heat transfer above a critical Reynolds number ($Re \geqslant 2800$) at $r/D \approx 0.5$ (primary maximum) and $r/D \approx 2$ (secondary maximum). The complementary work of Lee & Lee (1999) clearly shows that the amplitudes of these two maxima increase with the Reynolds number. The effects of the nozzle-to-plate distance (Baughn & Shimizu 1989), the nozzle type (Viskanta 1993; Roux *et al.* 2011) and the confinement (Obot, Douglas & Mujumdar 1982; Ashforth-Frost, Jambunathan & Whitney 1997) on the mean heat transfer distribution have also been studied experimentally. The main conclusions of these studies regarding the occurrence of a secondary maximum in the Nusselt number distribution are that the peak is more marked for a low nozzle-to-plate distance (typically $H/D \leqslant 3$) and using a convergent nozzle rather than a long tube at the inflow. The presence of a confinement plate is found to reduce the heat transfer on the impingement plate while being the most common geometrical configuration in practical applications.

In the work of Gardon & Akfirat (1965), the origin of the secondary maximum of the mean Nusselt number is attributed to the transition of the boundary layer from laminar to turbulent conditions. Then, further downstream of this laminar–turbulent transition, the decrease of the heat transfer is simply interpreted as the consequence of the mean radial velocity decrease to ensure mass conservation in the present axisymmetric flow. The connection between laminar–turbulent transition and the secondary peak of the Nusselt number is, however, questioned by the measurements of Cooper *et al.* (1993), showing that for a jet where the boundary layer is already turbulent in the stagnation region, the secondary maximum of $\langle Nu \rangle$ still exists. In their review paper, Jambunathan *et al.* (1992) propose that the secondary maximum is linked with the annular structures issuing from the jet shear layer. Using the flow visualisations of Popiel & Trass (1991), they also notice that secondary near-wall structures develop in the neighbourhood of the mean heat transfer secondary maximum location.

The investigations of Vejrazka *et al.* (2005), Buchlin (2011) and Roux *et al.* (2011, 2014) are in better agreement with the approach of Jambunathan *et al.* (1992), suggesting a strong relationship between the large-scale vortical structures and the secondary maximum of $\langle Nu \rangle$. Very few experimental studies deal with the unsteady analysis of the temperature field in the impinging jet flow (see Narayanan & Patil 2007; O'Donovan & Murray 2007). In the work of Roux *et al.* (2014), unsteady measurements of wall temperature for a round impinging jet at $Re = 28\,000$ with $H/D = 3$ and 5 are performed, and the convection of successive cold and hot thermal fronts is clearly observed at the same frequency as the near-wall structures. However, without synchronised velocity/temperature measurements, it is not possible to precisely link the vortex location to the increase or decrease in local heat transfer.

In the laminar case at low Reynolds number ($Re = 300$, 500, 1000), Chung & Luo (2002) and Chung, Luo & Sandham (2002) have shown by DNS that the secondary maximum of $\langle Nu \rangle$ can also be observed. According to these authors, the unsteady separation leads to an upstream thickening of the thermal boundary layer leading to a local minimum of $\langle Nu \rangle$, while at the location of the secondary vortex the thermal boundary layer is thinner leading to the secondary maximum of $\langle Nu \rangle$.

The LES of Hadziabdic & Hanjalic (2008) provides a comprehensive study of the heat transfer and its link with the vortical structures in the turbulent impinging jet flow. The instantaneous Nusselt number distribution is found to be very similar to that of the wall shear stress but with a phase shift. According to these authors, the local minimum observed before the secondary maximum is a consequence of the unsteady separation involving a thicker thermal boundary layer. The recirculating fluid is then trapped in the near-wall region and heated by the plate. The temperature of this fluid pocket is close to the temperature of the plate, leading to a local decrease of heat transfer. At slightly higher radial distance, the secondary peak of $\langle Nu\rangle$ is interpreted as the consequence of the unsteady reattachments of the boundary layer downstream of the unsteady separations.

The analysis of instantaneous fields issued from the low-Reynolds-number DNS ($392 \leqslant Re \leqslant 1804$) of Rohlfs *et al.* (2012) confirms, in agreement with Chung & Luo (2002), Chung *et al.* (2002) and Hadziabdic & Hanjalic (2008), that the secondary maximum is directly linked with the location of the secondary vortex. The additional interpretation provided by these authors is that the unsteady separation and reattachment of the flow alone should not explain the secondary maximum of the mean Nusselt number because the local increase and decrease of heat transfer tend to neutralise each other due to the convection of the secondary vortex. It is then suggested that the upward motion induced by the ejection of the secondary vortex can explain the secondary peak in the Nusselt number distribution.

A different interpretation of the origin of the secondary maximum has been proposed by Uddin *et al.* (2013). In their LES, they observe that the large-scale toroidal structures are responsible for strong intermittent flow accelerations and decelerations. According to this study, the secondary maximum is only the consequence of the strong acceleration of the boundary layer flow after the jet impingement. No secondary vortex and consequently no unsteady separation is observed in these LES. Moreover, the instantaneous Nusselt number distribution highlights regions of very high heat transfer denoted as cold spots. The authors then make the assumption that these regions are linked with radially elongated coherent structures.

1.3. *Present study*

As summarised in this introduction, the detailed understanding of the heat transfer distribution at the wall is an important problem from both fundamental and practical points of view. Despite the numerous studies dealing with the impinging jet flow and its related heat transfer at the wall, there are still fundamental understanding issues regarding the link between the vortical structures and the unsteady heat transfer in the stagnation region. The experimental and numerical studies where the origin of the secondary maximum of $\langle Nu\rangle$ is investigated are not entirely conclusive or reach conclusions that are not fully consistent with each other. For example, although it is very likely that the secondary vortex has an influence on the mean heat transfer distribution, it is still difficult to understand to what extent it leads to an increase or a decrease of the heat transfer at the wall. In the context of Reynolds-averaged Navier–Stokes (RANS) modelling, the ability to reproduce the secondary peak is very challenging. This is another explanation of why this specific flow configuration is a topic of interest for the fluids and heat transfer communities. In the example already discussed at the beginning of this introduction regarding the extreme sensitivity of the lifetime of aircraft turbine blades with respect to a small temperature variation, it can easily be understood why a better knowledge of the mechanisms that promote (or not) the occurrence of the secondary peak is also of industrial interest for the design of efficient cooling devices.

For technical reasons, experimental studies are often limited to a 2D description of the flow and have extreme difficulty in dealing with simultaneous velocity/temperature measurements. On the contrary, DNS/LES simulations are a means to explore the fully 3D instantaneous flow and its resulting heat transfer processes (Lesieur, Métais & Comte 2005; Sagaut 2005). However, for computational cost

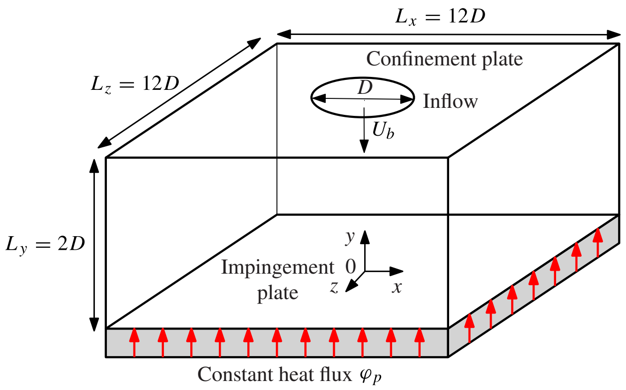

FIGURE 1. (Colour online) Schematic view of the flow configuration.

reasons, DNS studies have been limited to low-Reynolds-number flow ($Re < 3000$). For higher Reynolds numbers, only LES results are available in the literature, with the drawback that the subgrid-scale dynamics could play a significant role in the heat transfer processes while introducing extra uncertainty associated with the subgrid-scale modelling.

Taking advantage of the recent developments in high performance computing (HPC), a DNS of a turbulent impinging jet at $Re = 10\,000$ and $H/D = 2$ has been carried out in this work. The use of a very refined mesh, as required by DNS, enables the analysis of the full spectrum of time and space scales potentially involved in the flow dynamics and heat transfer. To the best of the authors' knowledge, this calculation is the first DNS of an impinging jet in a fully turbulent case. This flow configuration is designed to lead to a well-defined secondary maximum in the mean Nusselt number distribution. The main goal of the present study is to focus on the link between the unsteady flow and the heat transfer distribution at the wall. For that purpose, a consistent scenario regarding the mechanism of formation of the secondary peak in the mean Nusselt number distribution will be suggested and checked in terms of statistical relevance.

2. Flow configuration

A schematic view of the flow configuration is presented in figure 1. In the Cartesian coordinate system (O; x, y, z), the computational domain is $\varOmega = [-L_x/2, L_x/2] \times [0, L_y] \times [-L_z/2, L_z/2]$, where the origin O is located at the centre of the plate. For the sake of simplicity, the radial distance $r = \sqrt{x^2 + z^2}$ and the azimuthal angle $\theta = \arctan(x/z)$ are also introduced hereinafter (the reference plane $\theta = 0$ then corresponds to the plane $x/D = 0$ with $x > 0$). The Reynolds number of the flow is based on the jet diameter D and its (constant) bulk velocity U_b, with $Re = U_b D/\nu = 10\,000$, where ν is the (constant) kinematic viscosity. The Prandtl number is set to $Pr = \nu/\kappa = 1$, where κ is the (constant) thermal diffusivity of the fluid. This value has been chosen in order to be in the framework of the Reynolds analogy (not used here). It is also consistent with other numerical studies (e.g. Chung *et al.* 2002) and remains close to the usual experimental value ($Pr = 0.7$). The nozzle-to-plate distance H corresponds to the computational domain height L_y, with $H/D = 2$ for the case considered here.

The boundaries of the computational domain are composed of (i) the jet inlet at $y = L_y$ for $r \leqslant D/2$, (ii) the confinement plate $y = L_y$ for $r > D/2$, (iii) the impingement plate at $y=0$ and (iv) the outlets at $x=\pm L_x/2$ and $z=\pm L_z/2$. On the plates, no-slip boundary conditions are imposed for the velocity, whereas for the temperature, a constant heat flux is applied on the impingement plate while an isothermal condition is assumed on the confinement plate.

3. Numerical methods

The finite difference code 'Incompact3d' (Laizet & Lamballais 2009; Laizet, Lamballais & Vassilicos 2010) is used to solve the incompressible Navier–Stokes and temperature equations

$$\frac{\partial \boldsymbol{u}}{\partial t}+\frac{1}{2}\left(\nabla\cdot(\boldsymbol{u}\otimes\boldsymbol{u})+(\boldsymbol{u}\cdot\nabla)\,\boldsymbol{u}\right)=-\frac{1}{\rho}\nabla p+\nu\nabla^2\boldsymbol{u}, \tag{3.1}$$

$$\nabla\cdot\boldsymbol{u}=0, \tag{3.2}$$

$$\frac{\partial T}{\partial t}+\boldsymbol{u}\cdot\nabla T=\kappa\nabla^2 T, \tag{3.3}$$

where $\boldsymbol{u}=(u_x,\,u_y,\,u_z)^{\mathrm{T}}$ is the velocity, p is the pressure and T is the temperature. In the present framework, the density ρ is constant so that the temperature is only a passive scalar. The convective terms are written in the skew-symmetric form to enable reduction in aliasing errors and improvement of kinetic energy conservation for the spatial discretisation used in the code (Kravchenko & Moin 1997).

The computational domain $L_x\times L_y\times L_z=12D\times 2D\times 12D$ is discretised on a Cartesian grid of $n_x\times n_y\times n_z=1541\times 401\times 1541$ points. In order to concentrate the grid points near the impingement plate, the mesh is stretched in the axial direction y. Expressed in wall units at the radial location where friction velocity is maximum, this spatial resolution ensures $\Delta x^+=\Delta z^+\approx 10$ and $0.9\lessapprox\Delta y^+\lessapprox 40$. For the spatial derivatives, sixth-order centred compact schemes (Lele 1992) are used. To control the residual aliasing errors, a small amount of numerical dissipation is introduced only at scales very close to the grid cutoff. This very targeted regularisation is ensured by the differentiation of the viscous term that is sixth-order accurate (Lamballais, Fortuné & Laizet 2011). In practice, the amount of numerical dissipation provided by this discretisation is low and highly concentrated at small scale. It is mainly useful to control aliasing errors that are not negligible when high-order schemes are used and it avoids the occurrence of spurious grid-to-grid oscillations. However, if the spatial resolution is decreased too much, spurious oscillations are detected and the present regularisation technique is unable to control them. This behaviour has been shown in a recent LES study (Dairay *et al.* 2014) based on a coarser mesh where different subgrid-scale models were compared. For the case free from any explicit modelling (but using the same numerical dissipation as in the present DNS study), spurious oscillations are clearly observed and are found to strongly affect the heat transfer predictions.

The time integration is performed using a hybrid explicit/implicit third-order Adams–Bashforth/second-order Crank–Nicolson scheme with a time step $\Delta t=2\times 10^{-4}D/U_b$. In this study, the implicit treatment only concerns the second derivative in the stretched y direction. With such an explicit/implicit combination for the time advancement, the time step is only restricted by the Courant–Friedrichs–Lewy (CLF) condition. For this simulation, the maximum value of the CFL is equal to 90 % of the limit given by the stability analysis (CFL = 0.362), ensuring a good computational efficiency. For more information about the code 'Incompact3d', see

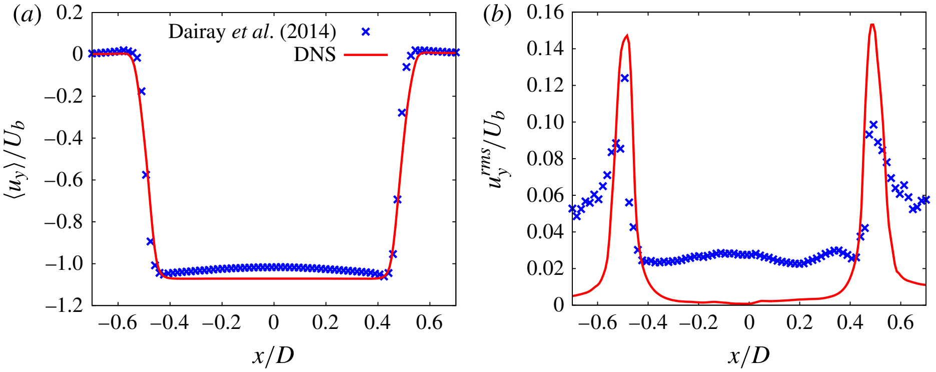

FIGURE 2. (Colour online) Mean (*a*) and r.m.s. (*b*) axial velocity profiles close to the jet inlet ($y/D = 1.7$) for the present DNS compared with the experimental data reported in Dairay *et al.* (2014).

Laizet & Lamballais (2009), Laizet *et al.* (2010) and also Laizet & Li (2011) concerning its massively parallel version available in code licence GNU GPL v3 (see the link http://code.google.com/p/incompact3d/).

No-slip boundary conditions are applied at the impingement plate $y = 0$ and at the confinement plate $y = L_y$ for $r \geqslant D/2$. To model the jet at the nozzle exit for $r < D/2$ at $y = L_y$, a mean velocity profile $\langle u_y \rangle$ is prescribed as inflow boundary condition,

$$\langle u_y \rangle = -\frac{n+2}{n}\left(1 - \left(\frac{2r}{D}\right)^n\right) U_b, \tag{3.4}$$

with n chosen in order to mimic a flat velocity profile associated with a short convergent nozzle that is well known to lead to a non-developed flow at the exit. The jet is excited using synthetic perturbations of the form

$$u' = f(r) \sum_{m=1}^{N} A_m(t) \cos\left(m\theta + \phi_m(t)\right) \tag{3.5}$$

for each velocity component, where N is the number of excited azimuthal modes and (A_m, ϕ_m) are the amplitude and phase generated randomly up to a cutoff frequency. The use of a limited number of azimuthal modes up to a moderate cutoff frequency avoids spurious excitations on space and time scales that cannot be accurately captured by the mesh. The exponent $n = 28$ in (3.4) and the modulation function $f(r) = A(R - r)\exp(-\sigma(R - r))$, where $A = 0.7\sigma \exp(1)$, $R = D/2$ and $\sigma = 1/(0.02R)$, in (3.5) are both adjusted to roughly match the experimental conditions previously reported in Dairay *et al.* (2014) for the same flow configuration (see figure 2 for illustration).

For the temperature field, a constant flux density $\varphi_p > 0$ is prescribed on the heated impingement plate with

$$\left.\frac{\partial T}{\partial y}\right|_{y=0} = -\frac{\varphi_p}{\lambda}. \tag{3.6}$$

The isothermal condition $T = T_j$ is prescribed on both the confinement plate and the jet inlet ($y = L_y$).

Near the lateral faces of the domain (i.e. $x/D = \pm L_x/2$ and $z/D = \pm L_z/2$), the fringe method proposed by Nordstrom, Nordin & Henningson (1999) is used. This technique consists in the addition of a volume force $\boldsymbol{F}$ on the right-hand side of the Navier–Stokes equations (3.1) with

$$\boldsymbol{F} = \lambda(r)\left(\widetilde{\boldsymbol{u}} - \boldsymbol{u}\right), \tag{3.7}$$

where $\widetilde{\boldsymbol{u}}$ is a target velocity field and $\lambda(r)$ is a modulation function allowing a local activation of the forcing in the region where $\lambda \neq 0$. As target velocity field, a purely radial flow is assumed with

$$\widetilde{\boldsymbol{u}} = \frac{3}{16}\frac{U_d D^2}{L_y r}\left(1 - \frac{4\left(y - L_y/2\right)^2}{L_y^2}\right)\boldsymbol{e_r} \tag{3.8}$$

where $\boldsymbol{e_r}$ is the unit vector in the radial direction. This artificial flow can be seen as a Poiseuille flow weighted with $1/r$ in order to ensure mass conservation and then avoid any conflict with the divergence-free condition (3.2). More details about the outflow boundary condition treatment by comparisons with a conventional radiative outflow condition can be found in Dairay *et al.* (2014). Concerning the temperature, a conventional convective outflow boundary condition is used.

It should be pointed out that despite the cylindrical nature of the mean flow configuration, a Cartesian mesh was preferred to a cylindrical one. The former is easy to implement without particular loss of accuracy due to the very low anisotropic errors provided by the high-order schemes used for the spatial differentiation. The latter requires a specific treatment for the singularity on the jet axis while resulting in a high concentration of mesh nodes near the centreline. This mesh node concentration is useless in terms of flow geometry while being computationally inefficient due to the extra constraint on the time step for numerical stability reasons. The main advantage of a cylindrical mesh is an easier implementation of the outflow boundary condition due to the shape of the computational domain which enables the mean flow direction to be perpendicular to the outlet. Because it was possible to overcome this difficulty using a buffer domain, the Cartesian mesh was considered to be the best option in terms of accuracy and computational efficiency.

In order to quantify the sensitivity of the heat transfer to the prescribed inlet mean velocity profile, an additional computation has been carried out using exactly the same parameters as the reference DNS reported in this paper but with an inlet velocity profile corresponding to a long tube injection. For that case, a turbulent pipe flow profile has been prescribed as in Lodato *et al.* (2009) with

$$\langle u_y \rangle = V_{max}\left(1 - \frac{2r}{D}\right)^{1/m}, \tag{3.9}$$

where V_{max} is the velocity on the jet axis and $m = 6.77$ (for $Re = 10\,000$) has been chosen following Lodato *et al.* (2009) to give the same ratio of bulk and centreline inlet velocities as in the experiments of Cooper *et al.* (1993). The radial distributions of the mean Nusselt number obtained using the inflow conditions (3.4) corresponding to a convergent nozzle and (3.9) corresponding to a long tube are plotted in figure 3. In agreement with the experimental observations of Viskanta (1993), Lytle & Webb (1994) and Roux *et al.* (2011), the Nusselt number distribution corresponding to the long tube injection inlet velocity profile exhibits a maximum at the stagnation point

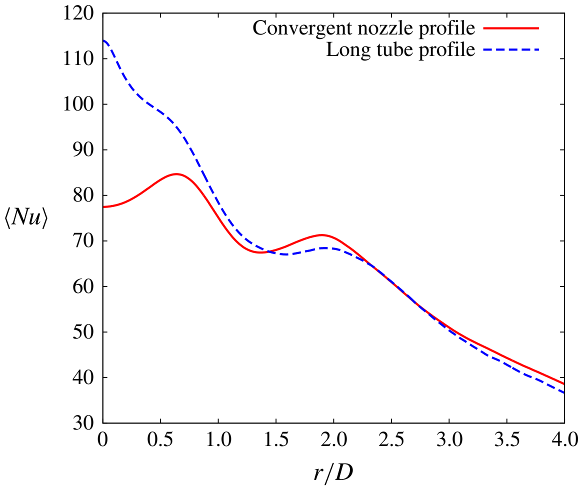

FIGURE 3. (Colour online) Radial distributions of the mean Nusselt number obtained when prescribing the inflow conditions (3.4) corresponding to a convergent nozzle and (3.9) corresponding to a long tube injection.

with a less marked secondary maximum compared with the convergent nozzle inlet velocity case. Because the main goal of this paper is to focus on the phenomena leading to the occurrence of a secondary maximum in the Nusselt number distribution and also because the convergent nozzle configuration is the most typical geometry in industrial applications, only the data of the DNS using the convergent nozzle profile (3.4) at the inlet will be considered in the following.

An experimental validation study of the present DNS has been carried out in Dairay *et al.* (2014) for both the velocity and temperature statistical fields. For illustration, radial velocity profiles at the location $r/D=2$ are plotted in figure 4 in comparison to the experimental data reported in Dairay *et al.* (2014) for the same flow configuration. A very good agreement between the calculation and experimental data of reference is found for the velocity statistics, particularly in the near-wall region of interest for this study. It should be pointed out here that the high fluctuation levels measured for $y/D > 0.6$ in figure 4(*b*) correspond to erroneous residual fluctuations which are directly linked to the limitations of the PIV measurement technique in the low-velocity regions. It is also worth mentioning that it was checked experimentally that buoyancy effects are negligible in the present flow configuration. The radial distribution of the mean Nusselt number is plotted in figure 5 following a normalisation proposed by Martin (1977) for the present DNS in comparison to the numerical data of Uddin *et al.* (2013) at $Re=13\,000$ and the measurements of Lee & Lee (1999) at $Re=10\,000$ with the same nozzle-to-plate distance $H/D=2$. Some differences can be noted between the three distributions regarding the stagnation point Nusselt number and the local maxima location. However, these are mainly assigned to differences in velocity inflow conditions between the studies and a good agreement is globally recovered for the mean heat transfer distribution.

In the demanding context of DNS, it is particularly important to check the adequacy of the spatial resolution for capturing with accuracy the full range of turbulent length scales involved in the flow dynamics. For that reason, the grid resolution has been compared with the Kolmogorov length scale $\eta=(\nu^3/\varepsilon)^{1/4}$, where

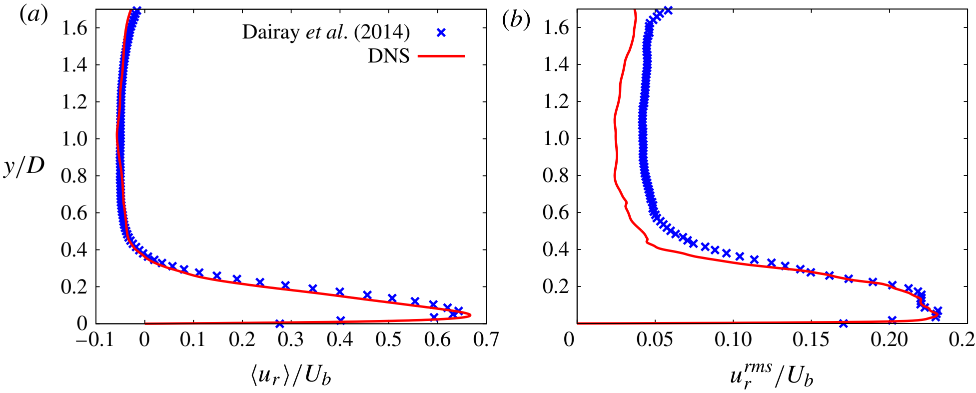

FIGURE 4. (Colour online) Mean (*a*) and r.m.s. (*b*) radial velocity profiles at $r/D = 2$ for the present DNS compared with the experimental data reported in Dairay *et al.* (2014).

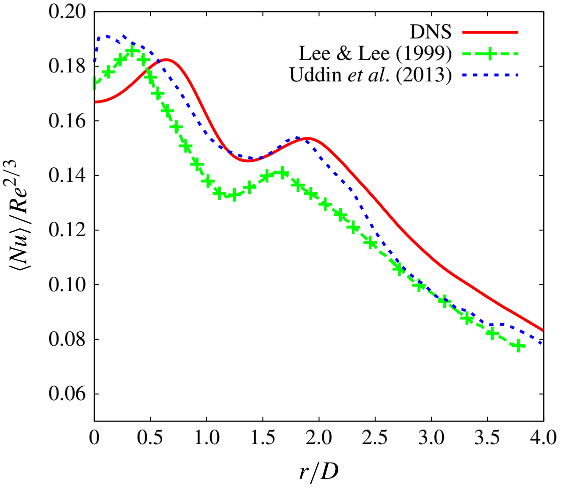

FIGURE 5. (Colour online) Radial distribution of the mean Nusselt number normalised by the Reynolds number of the flow for the present DNS compared with the numerical data of Uddin *et al.* (2013) and the experimental data of Lee & Lee (1999).

$\varepsilon = \nu \langle (\partial u_i'/\partial x_j)(\partial u_i'/\partial x_j) \rangle$ is the dissipation rate of the turbulent kinetic energy. A map of the ratio $\varDelta/\eta$ between the local mesh size $\varDelta = (\Delta x \Delta y \Delta z)^{1/3}$ and the Kolmogorov length scale η is plotted in figure 6. It can be seen that the mesh size is always smaller than 2η in the vicinity of the impingement plate ($y/D \leqslant 0.5$), with a maximum value of 7.58η close to the jet inflow where synthetic turbulent fluctuations are generated. These results meet the requirements for the DNS resolution as reported, for example, by Moin & Mahesh (1998).

4. Main turbulent statistics

Before analysing the unsteady flow and its related vortex structures, it is useful to provide a first insight into the main turbulent statistics for both the velocity and

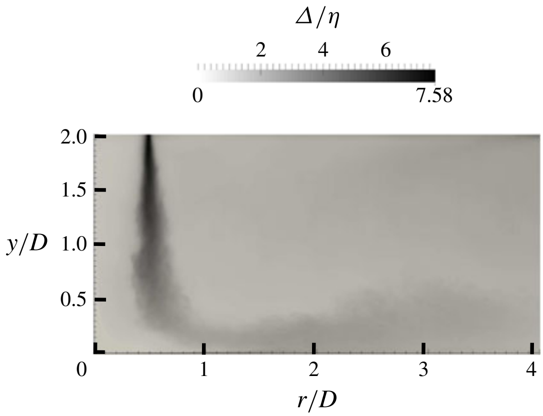

FIGURE 6. Map of the ratio Δ/η between the local mesh size $\Delta = (\Delta x \Delta y \Delta z)^{1/3}$ and the Kolmogorov length scale η.

temperature fields. In particular, it is interesting to examine to what extent the velocity statistics are connected to the temperature statistics.

The collection of data for the turbulent statistics is made over a period of 12 cycles, where the cycle period is evaluated from the estimated natural Strouhal number (based on U_b and D) $St \approx 0.4$ corresponding to the impinging frequency of the main large-scale structures in the jet. The mean quantity $\langle f \rangle(r, y)$ of a field $f(\boldsymbol{x}, t)$ is estimated by an average in time and in the homogeneous azimuthal direction. In a cylindrical coordinate system, in the absence of any swirl in the jet, the resulting mean velocity has two non-zero components $\langle u_r \rangle(r, y)$ and $\langle u_y \rangle(r, y)$ in the radial and axial directions respectively. At the wall, the efficiency of the heat transfer can be measured through the instantaneous Nusselt number defined as

$$Nu(r, \theta, t) = \frac{\varphi_p D}{\lambda \left(T_w(r, \theta, t) - T_j \right)}, \tag{4.1}$$

where $T_w(r, \theta, t)$ is the instantaneous wall temperature. The mean Nusselt number $\langle Nu \rangle$ is defined accordingly with

$$\langle Nu \rangle \, (r) = \frac{\varphi_p D}{\lambda \left(\langle T_w \rangle \, (r) - T_j \right)}, \tag{4.2}$$

where $\langle T_w \rangle(r)$ is the mean wall temperature.

Mean and fluctuating velocity components are presented in figures 7 and 8. The three main regions of the impinging jet flow are well recovered here despite the moderate value of the nozzle-to-plate distance $H/D = 2$. In the free jet region ($r/D < 0.5$ and $0.6 < y/D < 2$), the flow is mainly axial, as shown by figure 7(*b*). A potential core can be clearly observed with turbulent fluctuations that never exceed $0.05U_b$ on the jet centreline $r/D = 0$ (see figure 8). A shear layer located at $r/D \approx 0.5$ develops with turbulent fluctuation levels reaching $0.2U_b$ at $y/D \approx 0.8$ (see figure 8*b*). In the stagnation region ($r/D < 1.8$ and $0 < y/D < 0.6$), the comparison between the maps of $\langle u_r \rangle$ and $\langle u_y \rangle$ in figure 7 exhibits very well the change in the orientation of the mean flow from the axial to the radial direction. On the jet axis $r/D = 0$, the axial velocity starts to decrease at $y/D \approx 0.3$, with a sudden strong decrease in

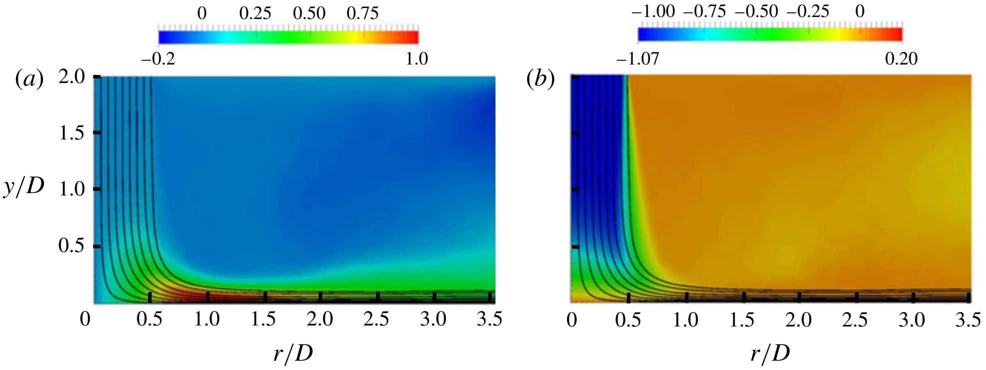

FIGURE 7. (Colour online) Maps of the radial $\langle u_r \rangle / U_b$ (*a*) and axial $\langle u_y \rangle / U_b$ (*b*) mean velocity components.

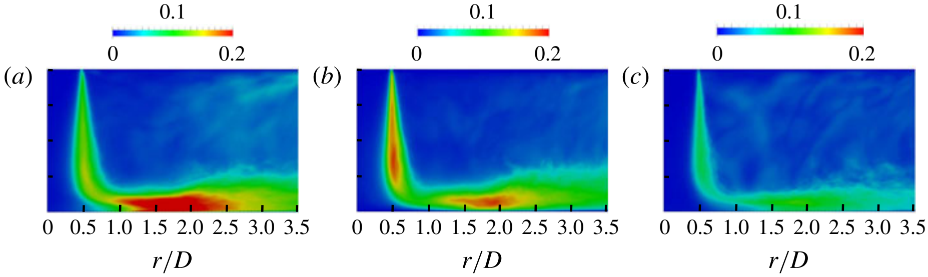

FIGURE 8. (Colour online) Maps of the radial u_r^{rms}/U_b (*a*), axial u_y^{rms}/U_b (*b*) and azimuthal u_θ^{rms}/U_b (*c*) r.m.s. velocity components. The axis label in the vertical direction y is the same as in figure 7.

the near-wall region up to the stagnation point. A wall jet flow then develops from the stagnation point and the radial velocity component increases, reaching almost the jet maximum velocity U_b at $r/D \approx 1$. The maxima of the velocity fluctuations are found in the stagnation region for the three components, with a maximum level of approximately $0.25U_b$ at $r/D \approx 1.8$ (see figure 8). In the wall jet region ($r/D > 1.8$), the flow becomes mainly radial. The wall jet thickness increases and the radial velocity component decreases with the radial distance for mass conservation reasons, as already stated.

In figure 9, the radial evolutions of the mean Nusselt number $\langle Nu \rangle$ and of the root mean square (r.m.s.) of the fluctuating temperature at the wall $T_w^{rms}(r) = \sqrt{\langle T'T' \rangle}$ are plotted together. Here, $\langle Nu \rangle$ is maximum at $r/D \approx 0.7$, with a local minimum at $r/D \approx 1.5$ and a secondary maximum at $r/D \approx 2$. For higher radial distances $r/D > 2$, $\langle Nu \rangle$ decreases monotonically as expected. In agreement with the observations made by Roux *et al.* (2011) for a jet issuing from a convergent nozzle with a small nozzle-to-plate distance ($H/D \leqslant 3$), the low level of fluctuations in the jet centre region (from the potential core region up to the impingement, see figure 8) is a feature that probably contributes to the establishment of a local minimum of the Nusselt number at the stagnation point.

In the impingement region ($0 \leqslant r/D \leqslant 0.5$), the wall temperature fluctuations consistently increase very slowly. The first peak of $\langle Nu \rangle$ at $r/D \approx 0.7$ seems to

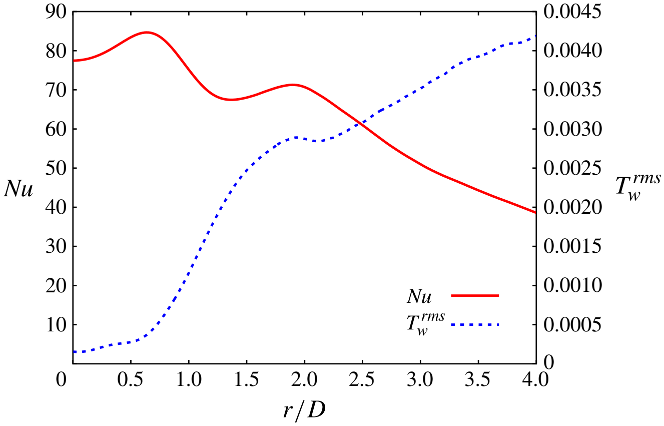

FIGURE 9. (Colour online) Radial distributions of the mean Nusselt number and temperature r.m.s. along the impingement plate.

correspond more to the location of the jet shear layer just above the impingement (after a slight radial expansion) than to a local production of strong temperature fluctuations. This production mechanism could, however, be suggested for the generation of the second peak of $\langle Nu \rangle$ at $r/D \approx 2$, where the T_w^{rms} also admits a local maximum. This location also corresponds to the high-turbulent-intensity region highlighted in figure 8. The convection of the structures issuing from the jet shear layer along the impingement plate can be given as a reason for this local production of turbulent fluctuations in the near-wall region (for both the temperature and the velocity), but the mechanism leading to the increase of the mean heat transfer in the range $1.5 \leqslant r/D \leqslant 2$ and the so-called secondary maximum appearance cannot be easily understood using only the present main statistics.

5. Instantaneous visualisations

To understand the origin of the secondary maximum of the mean Nusselt number, it is enlightening to identify the specific near-wall turbulent structures that drive the heat transfer processes in the stagnation region. In this section, instantaneous fields extracted from the present DNS database are used for that purpose. The Q-criterion is used as a vortex identification technique (Hunt, Wray & Moin 1988; Dubief & Delcayre 2000) with

$$Q = -\frac{\partial u_j}{\partial x_i}\frac{\partial u_i}{\partial x_j}. \tag{5.1}$$

First, to obtain a global perception of the flow structures, an isosurface of the Q-criterion in the full computational domain is presented in figure 10. The mainly toroidal organisation of the flow is clearly visible after the jet impingement. However, a fully 3D multiscale turbulence can also be detected in the near-wall flow with the presence of a wide population of thin vortex structures oriented in various directions. The analysis of a set of similar instantaneous visualisations suggests a qualitative decomposition of the unsteady near-wall flow into a large-scale component with quasi-toroidal structures and a small-scale component where the vortices are more oriented in the radial direction. This first insight has inspired the analysis presented in the rest of the paper.

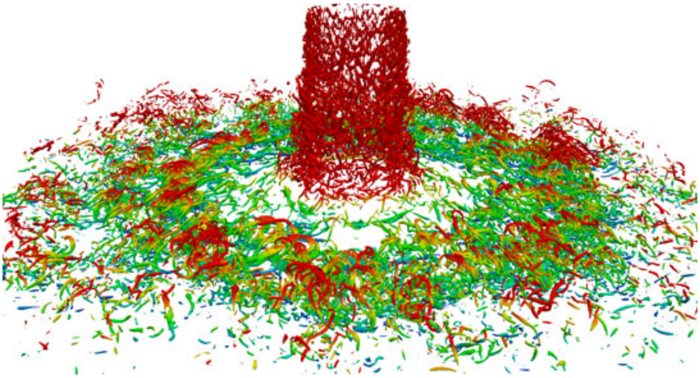

FIGURE 10. (Colour online) Isosurface of the Q-criterion ($Q = 100U_b^2/D^2$) in the full computational domain (excluding the fringe region). The colours correspond to the distance y/D from the impingement plate.

5.1. *Large-scale organisation*

As already discussed in the introduction, two types of large-scale toroidal structures develop in the wall jet region: the primary vortices originating from the jet shear layer and the counter-rotating secondary vortices in the near-wall region. These two opposite directions of rotation provide a simple way to distinguish primary and secondary toroidal vortices in a visualisation. For that purpose, a sign criterion can be based on the azimuthal component of the instantaneous vorticity,

$$\omega_\theta = \frac{\partial u_r}{\partial y} - \frac{\partial u_y}{\partial r}, \tag{5.2}$$

for which a positive/negative value can be associated with the direction of rotation of primary/secondary vortices respectively.

Visualisations of the Q-criterion isosurface coloured by the sign of the azimuthal vorticity are presented in figure 11. Using the perspective views in figure 11 (top), the stagnation zone of the flow can be divided into two regions: a near-wall region dominated by negative azimuthal vorticity, and further away from the wall, a region mainly occupied by vortical structures with a positive vorticity, including the vortices generated in the jet upstream from the impingement. Figure 11 (bottom) clearly shows that the mainly axisymmetric organisation of the flow at large scale concerns both the primary and secondary vortices. This selective detection based on the Q-criterion is a straightforward way to exhibit the interaction between secondary and primary vortices, as described by Didden & Ho (1985) and discussed in § 1. Despite the background small-scale 3D turbulence, the temporal evolution of visualisations similar to that presented in figure 11 shows that the formation of secondary vortices is synchronised with the primary vortex passing, with a slight shift in the radial direction. This typical organisation is summarised by the schematic view in figure 12.

The signature of these large-scale structures on the local heat transfer distribution can be seen in figure 13(a). Using instantaneous maps, the heat transfer distribution can be decomposed into two high-value regions. First, the high-Nusselt-number region located close to the jet impingement zone (at $0.5 \leqslant r/D \leqslant 0.7$) does not show any connection with the secondary structures such as $\omega_\theta < 0$ that are observed for higher radial distance. The first peak of the mean Nusselt number in this region is located

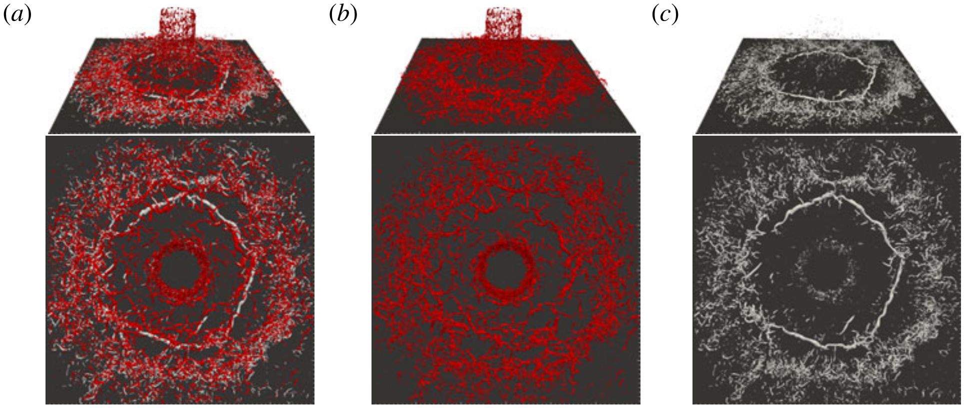

FIGURE 11. (Colour online) Isosurfaces of the Q-criterion ($Q = 100U_b^2/D^2$) coloured by the azimuthal vorticity ω_θ sign. Red represents $\omega_\theta > 0$ and grey represents $\omega_\theta < 0$. Full Q (*a*); Q such as $\omega_\theta > 0$ (*b*); Q such as $\omega_\theta < 0$ (*c*). The dimension of the subdomain plotted in this figure is $6D \times 2D \times 6D$.

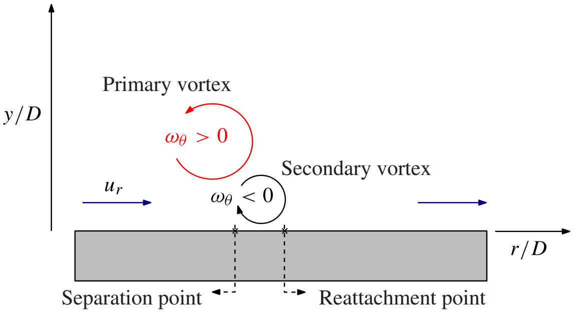

FIGURE 12. (Colour online) Schematic view of the large-scale organisation of the flow in the stagnation region.

in the zone of primary structure impingement (with positive azimuthal vorticity, see figure 11*b*). This qualitative observation is in agreement with the conclusion of Roux *et al.* (2011) whereby the primary maximum of $\langle Nu \rangle$ at $r/D \approx 0.7$ is interpreted as a consequence of the impingement of the primary structures ($\omega_\theta > 0$) issuing from the shear layer of the jet. The second region of high-Nusselt-number values is found close to the secondary structure ($\omega_\theta < 0$) location. This region of intense heat transfer is approximately located at $1.5 \leqslant r/D \leqslant 2$ (see figure 13), precisely in the zone of the second peak of $\langle Nu \rangle$ (see figure 9). It should be noted that even if only one instant is considered for the present analysis based on visualisation, it was checked that the same type of visualisation at other instants leads to the same qualitative conclusions concerning the strong connection between secondary vortices and high Nusselt number. Only the radial location is different depending on the progression of the secondary vortices at each instant while remaining in the range $1.5 \leqslant r/D \leqslant 2$.

5.2. *Small-scale organisation*

The pattern of the region of high instantaneous Nusselt number can be more easily identified if the map of Nu only shows the highest values. In figure 13(*b*), where only

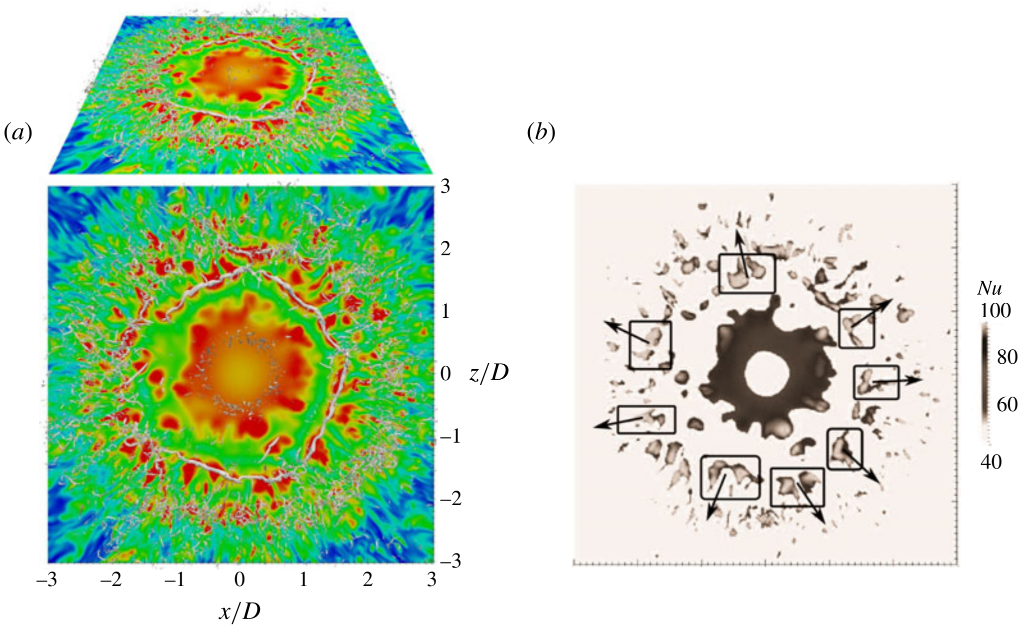

FIGURE 13. (Colour online) (*a*) Map of the instantaneous Nusselt number on the impingement plate ($y/D = 0$). The isosurface of the Q-criterion ($Q = 100U_b^2/D^2$) such as $\omega_\theta < 0$ is also presented. The colour map is saturated from $Nu = 30$ (blue) to $Nu = 90$ (red). (*b*) Map of the instantaneous Nusselt number high values ($Nu > 80$). The cold spots are represented inside black boxes and the black arrows show the radial elongation of the high-Nusselt-number regions.

regions with $Nu > 80$ are plotted, the corresponding heat transfer distribution does not exhibit the same azimuthal coherence as the large-scale quasi-toroidal secondary structures described in § 5.1. In particular, azimuthal locations for which the Nusselt number values are extremely high (black boxes in figure 13*b*) can be clearly observed. These regions can be referred to as cold spots for the present situation where the impingement plate is heated. In that case, the cold spots correspond to localised regions of the wall where the temperature is very low compared with the rest of the plate. The term 'cold' is thus relative to the temperature at the wall but not to the full temperature field, because the near-wall region, subjected to constant heat flux, is significantly warmer than the flow far from the wall, as expected. Similar spots have recently been observed in the simulations of Uddin *et al.* (2013). The cold spots are elongated in the radial direction, leading to a filament propagation of the heat transfer (black arrows in figure 13*b*). This phenomenon has already been observed by Hadziabdic & Hanjalic (2008) and Roux *et al.* (2014). In these previous studies, no link between the cold spots and a particular feature of the secondary vortices has been established.

Instantaneous flow visualisation can be insightful to connect the appearance of the cold spots (short azimuthal extension and radial elongation) with the near-wall structures of the flow. For that purpose, a map of the instantaneous near-wall temperature field in the plane $r/D = 1.5$ is plotted in figure 14. 'Mushroom-shaped' cold temperature zones can be clearly identified at different azimuthal locations (see figure 14*a*). On adding the isosurface of the Q-criterion (see figure 14*b*), it appears

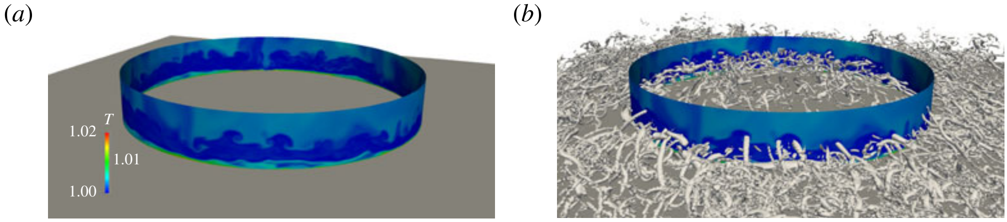

FIGURE 14. (Colour online) Instantaneous temperature field in the plane $r/D=1.5$ (*a*) and instantaneous temperature field in the plane $r/D=1.5$ plotted with the isosurface of the Q-criterion $Q=90U_b^2/D^2$ (*b*).

that these regions are the signature of radially elongated structures able to transport cold fluid towards hot regions, and *vice versa*.

A close examination of visualisations in perspective views, as for instance in figure 13(*a*) (top), does not suggest a direct link between the radially elongated structures and the cold spots. In terms of location, the cold spots are more related to the large-scale distortion of the secondary vortex. More precisely, the high-Nusselt-number regions are observed at azimuthal locations where the secondary vortex is the closest to the wall due to its wavy behaviour. Qualitatively, the role of the radially elongated structures seems to be more connected to the filament propagation of the cold spot regions further downstream of the secondary vortex.

To summarise, the pattern of the Nusselt number seems to be shaped by a combination of three mechanisms. The first mechanism corresponds to the formation of the secondary vortex that brings, as it rolls up, cold surrounding fluid towards the impingement plate. This mechanisms drives the time scale of the appearance of cold spots, but because it is essentially 2D (i.e. without azimuthal dependence), it cannot explain alone the strong azimuthal intermittency of the Nusselt number distribution. The latter can be interpreted as the consequence of a second mechanism for which the azimuthal distortion of the secondary vortex produces very high heat transfer in regions where it is the closest to the wall. The third mechanism, more difficult to evidence, involves the quasi-radial structures initially produced by vortex stretching between the main vortices. While wrapping around the secondary vortex, these structures are able to bring cold surrounding fluid towards the wall. In addition, because they are inclined with respect to the main flow direction, the resulting high heat transfer is shifted further downstream with a more elongated shape in the radial direction compared with the cold spots located just under the secondary vortex. These three mechanisms are sketched in figure 15.

5.3. *Spatiotemporal maps*

At this stage, the present analysis is mainly based on instantaneous visualisations. Even if it has provided a reasonable scenario to understand the physical processes responsible for the increase of the heat transfer in the region $1.5 \leqslant r/D \leqslant 2$, this analysis is essentially qualitative with potential bias through the selection of particular instantaneous fields. In the rest of the paper, a more quantitative investigation is presented while using this heat transfer scenario as a guide for the definition of significant criteria for the quantification.

Spatiotemporal monitoring of wall fields is another means to exhibit the link between the high-heat-transfer regions and the presence of the secondary vortex.

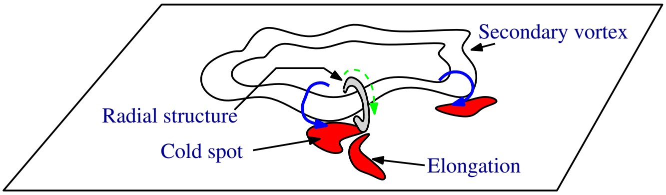

FIGURE 15. (Colour online) Sketch of the mechanisms involved in the appearance of cold spots in the instantaneous Nusselt number distribution. The blue solid arrows represent the cold fluid flow contribution due to the secondary vortex. The green dashed arrow represents the surrounding cold fluid flow contribution due to the radial structures.

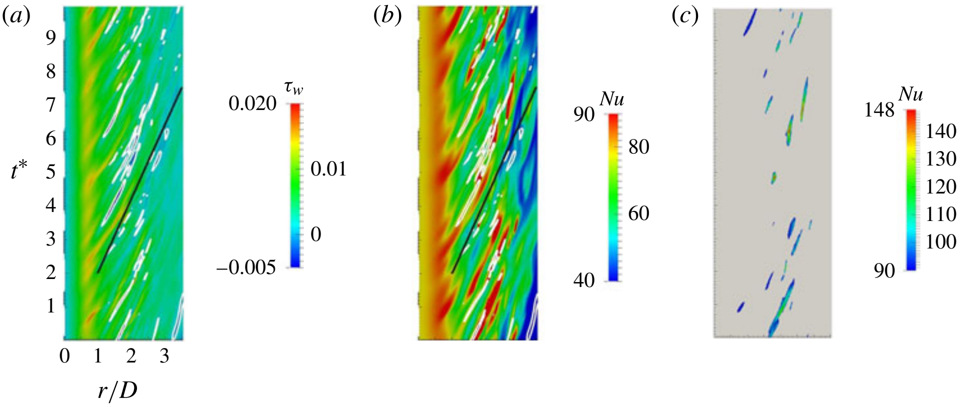

FIGURE 16. (Colour online) Spatiotemporal maps of the wall shear stress $\tau_w(r/D, \theta = 0, y/D = 0, t)$ (*a*), the Nusselt number $Nu(r/D, \theta = 0, y/D = 0, t)$ (*b*) and the high-Nusselt-number values $Nu \geqslant 90$ (*c*) in one radial direction on the plate. Isocontours of $\tau_w = 0$ are plotted in white in (*a*) and (*b*). The slopes of the two straight black lines correspond to the convection velocity $U_c = 0.45 U_b$.

Figure 16 presents (r, t) diagrams of the wall shear stress τ_w and Nusselt number Nu for a constant azimuthal location $\theta = 0$ (by convention). A comparison between the diagrams allows us to associate strong events of each quantity while better understanding the appearance of the mean Nusselt distribution plotted in figure 9.

First, in the region $r/D < 0.5$, the wall shear stress and Nusselt number are quasi-steady. The wall shear stress is close to $\tau_w = 0$ and the Nusselt number is $Nu \approx 80$. This region corresponds to the location of the local minimum of the mean Nusselt number observed in figure 9, where the turbulent fluctuations are very low due to the use of both a convergent nozzle inlet velocity profile and a small nozzle-to-plate distance. For $0.5 < r/D < 1$, the temporal evolutions are still weakly unsteady but with the regular occurrence of high values for both τ_w and Nu. This radial range includes the maximum of the mean Nusselt number $\langle Nu \rangle$ (see figure 9), where the near-wall turbulent fluctuations are high due to the jet shear layer. For $1 < r/D < 2.5$, negative regions of wall shear stress can be observed (identified by the white isocontours in figure 16). These negative shear stress events characterise a near-wall backward fluid flow that is associated with the formation of secondary vortices in the near-wall region.

A global similarity between the patterns of the τ_w and Nu diagrams can be drawn through a common convection velocity $U_c \approx 0.45U_b$ of the most intense events. The corresponding lines of characteristics $r - U_c t$ are plotted in figure 16. The present value of the convection velocity U_c is in good agreement with the measurements of Didden & Ho (1985) and Roux *et al.* (2011).

The comparative examination of the Nu and τ_w diagrams exhibits a clear correlation between high values of Nu and zones where $\tau_w \leqslant 0$. Cold fronts appear from $r/D \approx 1.5$ and are also convected at the velocity $U_c \approx 0.45U_b$. In figure 9, the location $r/D \approx 1.5$ corresponds to the location from which the mean Nusselt number increases again, reaching the secondary maximum at $r/D \approx 2$. Moreover, the spatiotemporal map in figure 16(*c*) shows that regions exist where the Nusselt number is particularly high ($Nu > 90$) in comparison with its mean value. These zones seem to be located on both sides of the secondary maximum location $r/D \approx 2$. These observations are additional confirmations of the strong link between cold spots and near-wall secondary vortices that is recovered here for the present time analysis.

To summarise, the present spatiotemporal maps of τ_w and Nu confirm that the region of the secondary maximum for the mean Nusselt number is strongly connected with the presence of secondary vortices. Cold fronts are convected at the same velocity as the secondary structure. Regions of extremely high values of the Nusselt number are detected in the neighbourhood of the secondary maximum location. In order to identify the physical mechanisms responsible for these extreme events, an analysis of the wall temperature distribution is presented in § 6.

6. Temperature distribution analysis

In this section, the probability density functions (PDFs) of the Nusselt number and the wall shear stress are computed at various radial locations. The goal is to better identify the regions where very high heat transfer occurs intermittently (in time and space) while examining their connection with the secondary vortex location and the resulting near-wall backward flow. The PDFs are calculated using 1000 temporal wall fields collected for a duration $T_f^* = 20D/U_b$ equivalent to eight periods of the main jet instability based on a natural Strouhal number $St_D = 0.4$.

The PDFs of the Nusselt number values in different radial ranges are plotted in figure 17. For $0 \leqslant r/D < 0.5$, Nu is weakly scattered around its mean value $Nu \approx 80$. For $0.5 \leqslant r/D < 1$, the scattering is significantly increased, with a slight asymmetry towards high values and a shift of the mean close to the primary maximum of the mean Nusselt number measured at $r/D \approx 1.7$. The region $1 \leqslant r/D < 1.5$ corresponds to the zone around the local minimum of $\langle Nu \rangle$. The most probable value is then translated to a lower value ($Nu \approx 65$) with a PDF that is more scattered and asymmetric. These two effects are clearly accentuated for $1.5 \leqslant r/D < 2$ and $2 \leqslant r/D < 2.5$, with no significant modification of the maximum of the PDF, which remains located at $Nu \approx 65$. For these two radial ranges, surrounding the secondary peak of $\langle Nu \rangle \approx 70$, the PDFs of Nu are highly skewed due to the development of an exponential tail up to very high values, $Nu > 250$. It can be expected that the occurrence of the corresponding rare but extremely intense thermal events has a non-negligible contribution to the mean Nusselt number. Physically, this indicates that cold spots (associated with high Nu) are very intermittent, in contrast to low-Nu regions. Finally, for $2.5 \leqslant r/D < 3$, the Nusselt number PDF tends to be symmetric again and the most probable value decreases to $Nu \approx 45$. This region corresponds to the monotonic decrease of the mean Nusselt number.

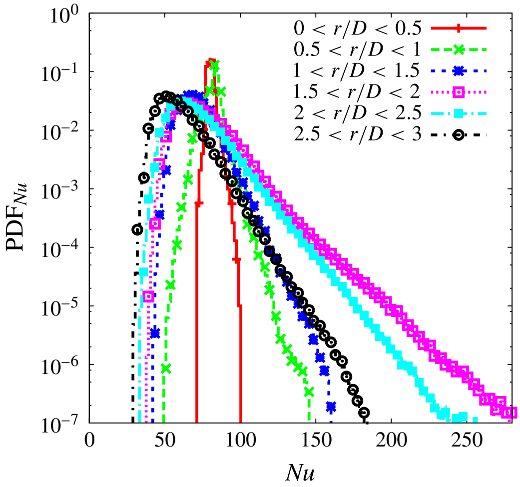

FIGURE 17. (Colour online) Probability density functions of the Nusselt number values in different regions of the impingement plate (linear–logarithmic scale).

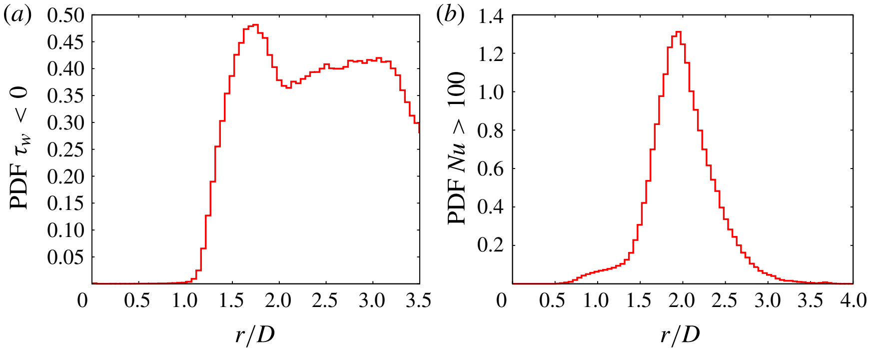

FIGURE 18. (Colour online) Probability density functions of the events $\tau_w \leqslant 0$ (a) and $Nu \geqslant 100$ (b) with respect to the radial location r/D.

To connect the strong thermal events with the flow dynamics, it is interesting to investigate the occurrence of the near-wall secondary vortex. As the visualisations of § 5.1 clearly highlight a 2D toroidal main flow, the simple criterion $\tau_w \leqslant 0$ is used here to detect the near-wall backward flow related to the appearance of the secondary vortex. The PDFs of the events $\tau_w \leqslant 0$ with respect to the radial location r/D are presented in figure 18(a). Up to $x/D \approx 1$, no secondary vortex is detected, in agreement with the observations based on visualisation. The most probable events are located in the range $1.5 \leqslant r/D \leqslant 2$, with a well-marked PDF peak at $r/D = 1.7$. This location is consistent with the analysis based on visualisation, where the presence of the secondary vortex (associated with a local separation) was detected in this region. This range corresponds also to the region where the PDF of the Nusselt number (see figure 17) is the most skewed towards very high values. Another way to locate the strongest thermal event is to consider the PDF of the condition $Nu > 100$ against the radial location (see figure 18b). It can be observed that these extreme events are localised in the same range $1.5 \leqslant r/D \leqslant 2.5$, with a maximum probability at $r/D \approx 2$.

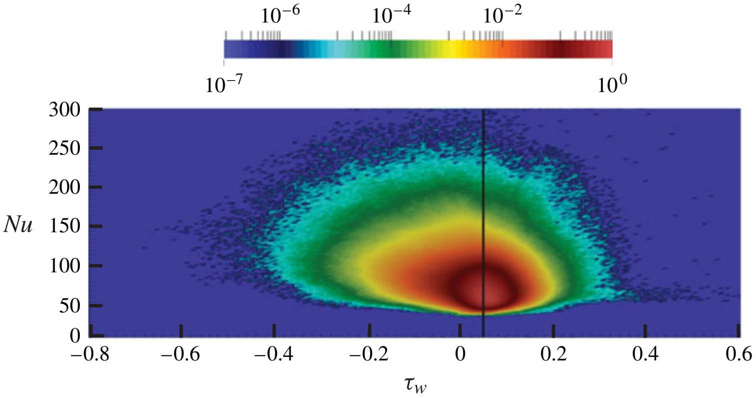

FIGURE 19. (Colour online) Joint PDF of the Nusselt number and wall shear stress values in the range $1.5 \leqslant r/D \leqslant 2$. The black vertical solid line corresponds to the mean value of the wall shear stress, $\langle \tau_w \rangle D/U_b = 0.004782$.

This location is slightly downstream of the peak observed at $r/D = 1.7$ for the PDF of τ_w. The present comparison between the PDFs of τ_w and Nu exhibits the link between the formation of secondary vortices (slightly downstream of an unsteady separation) and the appearance of a secondary maximum on the radial evolution of the Nusselt number. More precisely, it corresponds to the location where the probability of intense heat transfer occurrence is maximum. Presumably, these thermal events are related to the appearance of very localised cold spots in the instantaneous Nusselt number distribution highlighted using instantaneous visualisations in § 5.

Up to this stage, this link between τ_w and Nu is only based on the good matching between the radial locations of the highest probability of near-wall backward flow and intense heat transfer. To establish more clearly the connection between these two types of event, the joint PDF of τ_w and Nu is presented in figure 19 for the radial range $1.5 \leqslant r/D \leqslant 2$. The strong asymmetry with respect to the vertical axis, $\langle \tau_w \rangle D/U_b = 0.004782$ (which corresponds to the mean value of τ_w in this zone), confirms the occurrence of strong near-wall backward flow, with a non-negligible statistical contribution regarding their significant probability. In addition, these strong events are found strongly correlated with high values of Nu, as shown by the extended left wing of the joint PDF which is shifted upward with respect to its right counterpart (see figure 19). This particular pattern for the joint PDF of τ_w and Nu confirms the significant statistical contribution of events simultaneously combining separation (associated with the backward flow due to the presence of the secondary vortex) and very high heat transfer.

The estimation of the actual contribution of very intense thermal events to the mean value of the Nusselt number could be performed easily through a partial integration of the PDF of Nu from a lower limit chosen arbitrarily (for instance, from $Nu = 100$ in the range $1.5 \leqslant r/D \leqslant 2$). Here, this point is investigated in another way by wondering how the mean heat transfer would be without the strongest thermal events. For that purpose, PDFs of the Nusselt number have been computed at 13 different radial locations on the plate for $r/D = \{0; 0.25; 0.5; \ldots; 3\}$. The mean Nusselt number distribution obtained after temporal averaging of the probe data is presented in figure 20 (red solid line). Despite a marginal statistical convergence, the radial distribution of figure 9 is recovered up to the secondary maximum located at

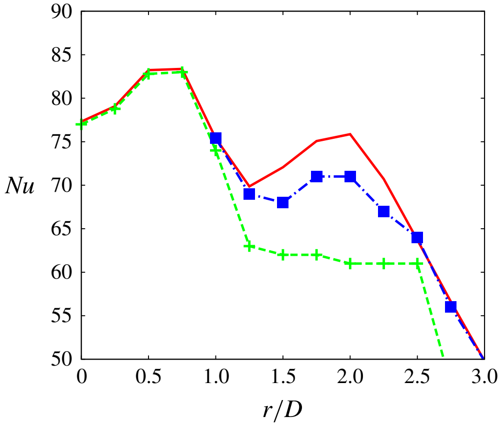

FIGURE 20. (Colour online) Radial evolutions of the mean Nusselt number (red solid line), the most probable Nusselt number (green dashed line with cross symbols) and the most probable Nusselt number of the residual PDF (blue dash-dotted line with square symbols).

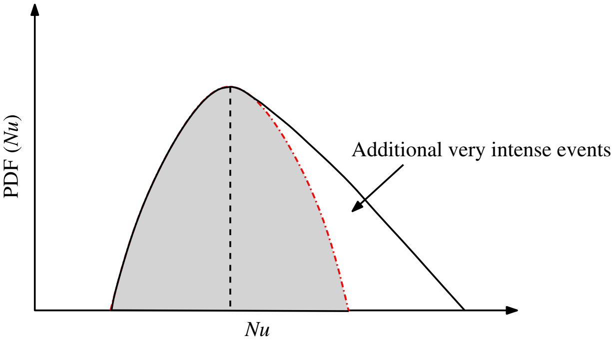

FIGURE 21. (Colour online) Sketch of the Nusselt number PDF decomposition. The black solid curve is the base PDF. The black dotted line is the location of the PDF maximum. The red dash-dotted curve corresponds to the symmetrical part of the PDF with respect to the PDF maximum location.

$r/D \approx 2$. Here, we focus on the range $1.25 \leqslant r/D \leqslant 2$, which corresponds to the zone where the mean heat transfer increases with the radial distance. In order to quantify the role of the extreme events, a very simple decomposition of the Nusselt number PDFs can be performed by distinguishing the mean and most probable values of the Nusselt number at each location. The mean Nusselt number would indeed be equal to the PDF maximum if the PDF was symmetric, as it is sketched in figure 21. Then, comparison of the mean and most probable values is a straightforward way to estimate the contribution of intense thermal events as the difference between these two values. The resulting decomposition corresponds to a split of the PDF into a symmetric part and a residual part. These two Nusselt numbers (most probable and mean values) are plotted in figure 20. In the range $0 \leqslant r/D \leqslant 1$, as was already noted in figure 17, the symmetry of the PDF (with respect to its maximum) provides a negligible residual asymmetric part with virtually no difference between the most probable and mean

Nusselt numbers. On the contrary, in the range of interest $1.25 \leqslant r/D \leqslant 2.5$, the most probable value of Nu (which can be interpreted as the mean of the symmetric part of its PDF) is almost constant ($Nu \approx 62$) for the radial locations considered. By the difference from the actual mean value $\langle Nu \rangle$, it can be concluded that the increase of the mean Nusselt number is due to additional extreme events in heat transfer which can contribute strongly to the overall heat transfer despite their highly intermittent nature. Further downstream, the residual asymmetric part of the PDFs vanishes so that the most probable and mean Nu match again for $r/D = 3$.

The present simple symmetric/asymmetric decomposition of the PDF can be performed iteratively on each residual part obtained by subtraction of the symmetric part (red dash-dotted curve in figure 21) from the base PDF (black solid curve in figure 21). The residual PDF also has a symmetric part with respect to its maximum and can be decomposed as the native PDF, and so on and so forth. In this iterative procedure, the most probable value of the final residual PDF corresponds to the mean value associated with the native data. In practice, only two iterations are necessary to obtain a secondary peak of the Nusselt number at $r/D \approx 2$, as shown in figure 20 (blue curve with square symbols). This means that the capture of the strongest events is not required to reproduce the local increase of the Nusselt number in the range $1.5 \leqslant r/D \leqslant 2$. However, the residual most intermittent events are not negligible, with a contribution of 7 % to the secondary peak of $\langle Nu \rangle$, which corresponds to approximately 60 % of its local increase.

Using the present decomposition, the mean heat transfer distribution at each radial location can be seen as the sum of symmetric PDFs. The first PDF is symmetric with respect to the maximum of the native PDF, and the radial evolution of the corresponding Nusselt number is constant in the range $1.5 \leqslant r/D \leqslant 2$. It seems reasonable to associate this behaviour with the passing of primary vortices and the formation of secondary vortices that generate alternating hot and cold fronts (see the spatiotemporal maps in figure 16) with a strong axisymmetric component. Because these vortices are convected radially, their thermal signature leads to constant heat transfer after time averaging. On the contrary, when the symmetric part of the first residual PDF is considered, the radial evolution of the Nusselt number recovers its typical shape, with an increase in the range $1.5 \leqslant r/D \leqslant 2$ and a secondary peak located at $r/D \approx 2$. About half of the bump amplitude can be reproduced after this second decomposition. Again, it seems reasonable to attribute this secondary maximum to the occurrence of cold spots previously observed by visualisation. Because these cold spots correspond to strong deviations from axisymmetry in the heat transfer, they are driven by strongly 3D events in the vortex dynamics. Finally, the present quantitative decomposition shows that the most intermittent turbulent events cannot be neglected in the heat transfer contribution. This conclusion can explain why the second peak on the mean Nusselt number radial distribution is so difficult to capture in the context of RANS (Manceau, Carpy & Alfano 2002; Dewan *et al.* 2012).

7. Conditional averaging of temperature and velocity

The previous analysis based on PDFs enables a quantitative distinction between more or less strong and intermittent events in the heat transfer. However, a vortex-blind analysis can only be speculative for the connection of these events with the flow dynamics. The instantaneous visualisations discussed in § 5 have offered some reasonable scenarios for the physical processes involved in the local heat transfer, but with a lack of proof in terms of statistical relevancy. In order to consolidate the present interpretation concerning the link between the vortical events and the local heat transfer, a statistical reconstruction of the flow topology in the neighbourhood of a cold spot is proposed. The methodology is very close to that of used, for example, by Blackwelder & Kaplan (1976) or Kim (1985) to study the burst phenomena in turbulent boundary layers and referred to as variable-interval time averaging (VITA)/variable-interval space averaging (VISA) algorithms.

7.1. *Cold spot detection and conditional averaging*

Considering the previous PDF analysis, it appears that the most intense thermal events are mainly detected in the range $1.5 \leqslant r/D \leqslant 2$. For that reason, we consider the intermediate radial location $r/D = 1.75$. In the neighbourhood of this radial location, using instantaneous snapshots, the various instants for which intense thermal events occur are identified. For illustration purposes, the temporal evolution of the azimuthally averaged Nusselt number is plotted in figure 22(*a*), where six local maxima are detected (black squares). In the following, only the instants where the azimuthally averaged Nusselt number reaches a local maximum (the black squares in figure 22) are selected for the averaging procedure. The azimuthal averaging procedure is performed only to detect the instants of intense thermal events. Then, for every time detected, the fully 3D instantaneous fields are considered.

Thereafter the methodology is based on two steps for each selected snapshot: (i) detection of the azimuthal angles corresponding to a cold spot; (ii) reconstruction of the aerothermal fields in the vicinity of the cold spot using conditional averaging. By repeating this process for each of the selected snapshots and performing temporal averaging of the conditional fields, the typical organisation (in the present statistical sense) of the flow in the high-heat-transfer regions can be obtained.

The azimuthal evolution of the Nusselt number is plotted in figure 22(*b*) (red solid curve) for one of the selected snapshots. As it is difficult to isolate cold spots using a simple threshold criterion based on the instantaneous data, a filtering based on a moving average at the location $r/D = 1.75$ is performed through the operator

$$\widehat{Nu}\,(\theta, t_0, L_\theta) = \frac{1}{L_\theta} \int_{\theta - L_\theta/2}^{\theta + L_\theta/2} Nu(\xi, t_0)\,\mathrm{d}\xi, \tag{7.1}$$

where t_0 is the instant corresponding to the selected snapshot and L_θ (angle) is the width of the angular window used to compute the average. Using this averaging, the more regular pattern of the data (see the blue curve in figure 22*b*) enables an unambiguous detection of the cold spots simply based on a threshold criterion applied to the filtered Nusselt $\widehat{Nu}$. Formally, the detection function is

$$D(\theta) = \begin{cases} 1 & \text{for } \widehat{Nu}(\theta) > S, \\ 0 & \text{otherwise}, \end{cases} \tag{7.2}$$

where S is a constant threshold value that selects the highest peaks in the filtered Nusselt number distribution $\widehat{Nu}$. With this definition, the cold spots are simply localised at angles θ_j where $D(\theta) = 1$.

Once the azimuthal locations of the cold spots have been detected, a conditional averaging of the flow fields is performed. For a scalar function $f(r, \theta, y, t_0)$, the

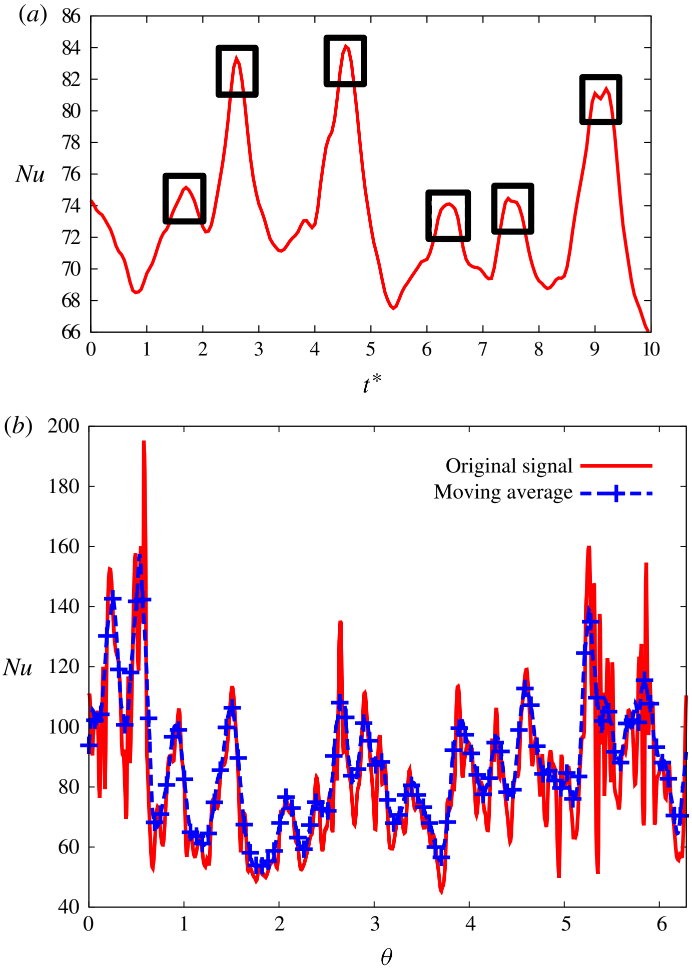

FIGURE 22. (Colour online) Temporal evolution of the azimuthally averaged Nusselt number at the radial location $r/D = 1.75$ (*a*) and example of the azimuthal distributions of the Nusselt number for one selected snapshot (*b*). The red solid curve is for the instantaneous Nusselt number Nu and the blue dashed curve with cross symbols is for the Nusselt number obtained after performing a moving average $\widehat{Nu}$ with $L_\theta = \pi/25$.

corresponding operator can be defined as

$$\langle f(r, \xi, y, t_0)\rangle_{Nu} = \frac{1}{N}\sum_{j=1}^{N} f(r, \theta_j + \xi, y, t_0), \tag{7.3}$$

where N is the total number of detected cold spots and θ_j is their azimuthal location. Finally, by performing temporal averaging of each conditionally averaged field, a statistical reconstruction of the flow in the neighbourhood of a cold spot is obtained. The expected azimuthal symmetry of the present conditional average is also applied to improve the statistical convergence.

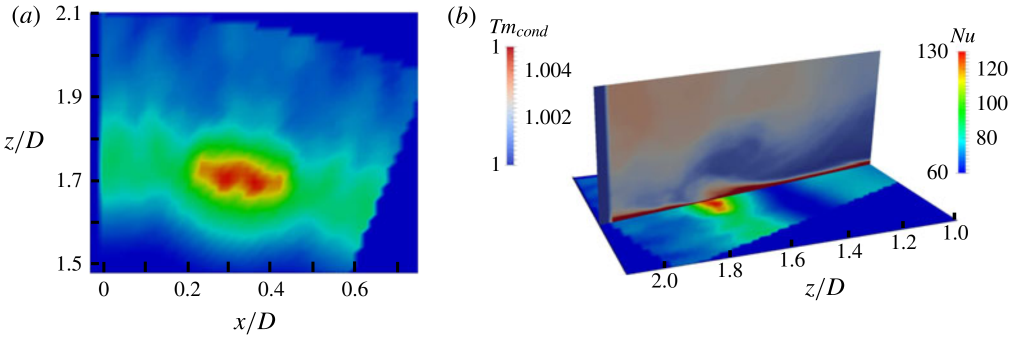

FIGURE 23. (Colour online) Map of the conditional Nusselt number distribution $\langle Nu(r,\theta)\rangle_{Nu}$ alone (*a*) and with a map of the conditional temperature field $\langle T(r,\theta,y)\rangle_{Nu}$ in the plane $\theta=0$ (*b*).

7.2. *Aerothermal fields in the vicinity of a cold spot*

The conditional mean fields obtained using the method described in the previous subsection are presented here. To detect the cold spots, the threshold value is set at $S=110$. This value has to be chosen as a compromise to ensure a maximal number of detections (to reach a significant statistical convergence) while isolating the cold spots from the background turbulent events in the heat transfer. In figure 17, for the corresponding radial location, the development of the exponential tail can be observed beyond this value, suggesting that the detection is triggered only for intermittent events. By convention, the azimuthal plane of reference is denoted $\theta=0$ and corresponds to the plane where the conditional mean Nusselt number reaches its maximum at the location $r/D=1.75$.

The conditional mean Nusselt number is presented in figure 23(*a*). The isolated cold spot is clearly visible and takes values between $\langle Nu\rangle_{Nu}=110$ and $\langle Nu\rangle_{Nu}=130$. A map of the conditional mean temperature in the azimuthal plane of reference ($\theta=0$) is also shown in figure 23(*b*). The thermal signatures of both the primary and secondary vortices can clearly be seen on the temperature map. The pattern of the conditional mean temperature also highlights a cold fluid flux pointed towards the location of the cold spot.

To confirm the presence of a near-wall backward flow at the cold spot location, the radial distribution of the conditional radial velocity component is plotted together with the conditional Nusselt number in figure 24 at the near-wall location $y/D=(\Delta y/D)_{min}$ and for the azimuthal angle of reference $\theta=0$. The conditional radial velocity shows a clear backward motion of the flow on either side of the Nusselt number maximum location. A global vision of the flow in the vicinity of the cold spots is given by the conditional mean streamlines plotted in figure 25(*a*) in the azimuthal plane of reference $\theta=0$. It should be noted that due to the symmetry expected for the present flow and the conditional average technique, these are not the projected streamlines but the actual ones due to the lack of any azimuthal velocity in this particular plane. The resulting pattern enables the clear identification of primary and secondary vortices. The secondary vortex is detected very close to the cold spot location while being of small size. This conditional mean vortex can be seen as a recirculation bubble enclosed between a flow separation and reattachment. The resulting conditional flow field can be interpreted as the typical unsteady separation that occurs periodically in this region although the mean flow is fully attached. Further from the wall, the primary

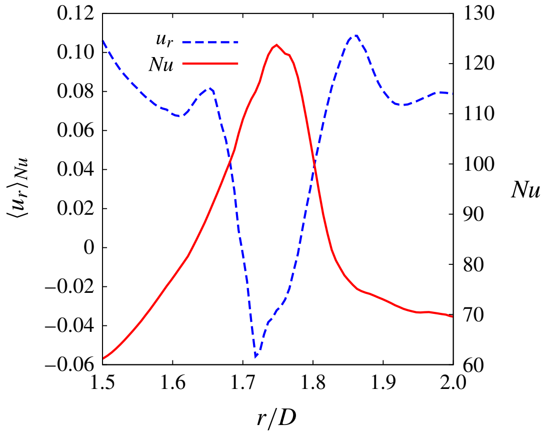

FIGURE 24. (Colour online) Radial distribution of the conditional Nusselt number $\langle Nu \rangle_{Nu}$ plotted together with the conditional radial velocity $\langle u_r \rangle_{Nu}$ component at the location $y/D = (\Delta y/D)_{min}$ and $\theta = 0$.

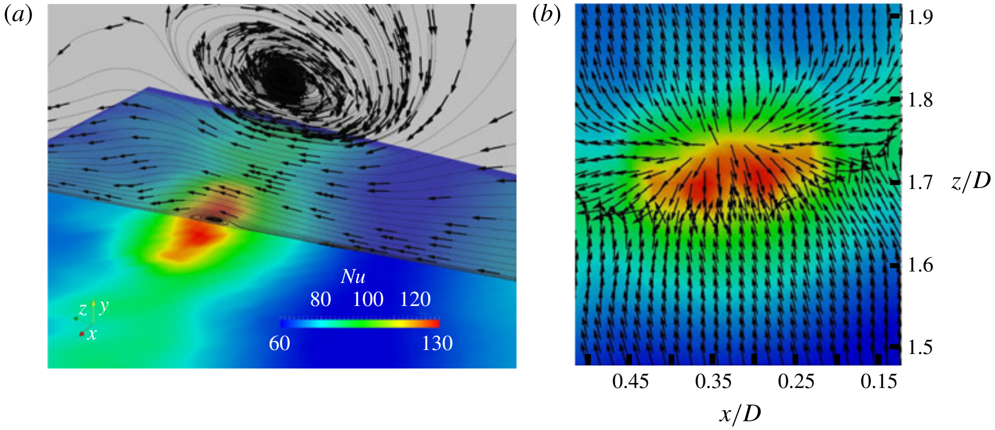

FIGURE 25. (Colour online) Conditional Nusselt number distribution $\langle Nu \rangle_{Nu}$ with streamlines of the conditional velocity field $\langle \boldsymbol{u} \rangle_{Nu}$ projected in the plane $\theta = 0$ (*a*) and with projected velocity vectors in the near-wall plane $y/D = (\Delta y/D)_{min} = 1.5 \times 10^{-3}$ (*b*).

vortex is clearly larger with a direction of rotation that is the same as the vortical structures issuing from the jet upstream of the impingement. The detected secondary vortex is counter-rotating, as expected.

Because cold spots are highly localised in the azimuthal direction, it can be expected that the conditional mean velocity field has a significant 3D component in the secondary vortex region. This feature is illustrated in figure 25(*b*) where the corresponding projected velocity vectors are plotted in the near-wall plane $y/D = (\Delta y/D)_{min}$. It can be observed that the cold spot is well located just below the secondary vortex with a pattern that enables the clear identification of a backward fluid motion but also the presence of a 3D motion in the vicinity of the cold spot.

To conclude this section, it is worth noting that the present conditionally averaged aerothermal fields representing the high-heat-transfer regions have a number of common characteristics with the instantaneous fields analysed in § 5. First, the velocity field corresponding to the high-Nusselt-number values shows the signature of a near-wall vortical structure such as $\omega_\theta < 0$ (secondary vortex) with a large-scale structure (primary vortex) located above it, the former being counter-rotating with respect to the latter. The associated temperature field exhibits a cold fluid flux towards the impingement plate. The velocity of the secondary vortex induces this convective flux. The Nusselt number is then maximum between the separation and reattachment lines of the secondary vortex.

The present conditional mean results show that the role of the secondary vortex, already highlighted by instantaneous visualisation (see § 5), is also statistically representative of the flow in the vicinity of a cold spot. Moreover, the cold spot topology presented in figure 23(*a*) confirms their intermittent character in the azimuthal direction which strongly breaks the axisymmetry of heat transfer processes.

8. Conclusion

Direct numerical simulation of an impinging jet at $Re = 10\,000$ and $H/D = 2$ has been carried out for the first time in a fully turbulent flow regime. The study is focused on the link between the vortical structures and the secondary maximum observed in the radial distribution of the mean Nusselt number. In particular, as the increase of the mean heat transfer in the range $1.5 \leqslant r/D \leqslant 2$ is difficult to understand by investigating only the mean flow, the space- and time-resolved DNS results were used to analyse the main unsteady features of the flow.

In agreement with the documented experimental results, the instantaneous visualisations evidence the large-scale organisation of the flow in the impingement region and further downstream. Among the main turbulent structures, two types of large-scale structures can be distinguished: (i) the primary vortices issuing from the upstream jet and evolving in the outer layer of the flow downstream of the impingement; (ii) the secondary vortices that are generated in the near-wall region of the flow. The primary and secondary vortices are counter-rotating with a mainly toroidal organisation. In this study, a small-scale organisation composed of multiple radially elongated structures is also highlighted. These structures are azimuthally distributed all around the toroidal vortices. Concerning the temperature field at the wall, the large-scale organisation of the flow is connected with the ring propagation of cold (high Nusselt number) and hot (low Nusselt number) fronts. A more subtle influence on the heat transfer is related to the small-scale component of the dynamics, which leads to the occurrence of radially elongated cold spots (localised angular and radial regions of intense heat transfer) clearly observable in the instantaneous Nusselt number distribution.

The investigation based on instantaneous flow visualisation provides a phenomenological scenario to explain the mean heat transfer increase in the range $1.5 \leqslant r/D \leqslant 2$, leading to the secondary maximum of the Nusselt number at the radial location $r/D = 2$. First, the convection of the primary and secondary vortices is directly linked with the ring propagation of hot and cold fronts of the Nusselt number. The highest-heat-transfer regions are located in the region of formation of secondary vortices whose induced velocity generates a convective flux of cold fluid towards the impingement plate. Second, superimposed on their toroidal structures, these secondary vortices are subjected to azimuthal distortions that lead to angular locations where they are locally closer to the wall. These regions correspond to the cold spots of the Nusselt number where the heat transfer is particularly high. It can be suggested that the azimuthal distortion of the secondary vortex is driven by a secondary instability mechanism in the same way as for the impingement of an isolated ring vortex on a plate (Walker *et al.* 1987; Orlandi & Verzicco 1993; Swearingen, Crouch & Handler 1995). As a third influence, radially elongated structures located in the neighbourhood of the cold spots also carry cold fluid from the surrounding flow towards the wall, explaining the so-called filament propagation of the heat transfer.

The analysis of spatiotemporal maps of the Nusselt number and the wall shear stress combined with the investigation of the wall temperature distribution provides more quantitative elements on the physical mechanisms involved in the heat transfer. First, the spatiotemporal maps confirm that the cold fronts are actually convected at the same velocity U_c as the secondary vortex, with a value $U_c = 0.45U_d$ in agreement with the documented experimental results. The PDF analysis of the Nusselt number values shows that extremely high values can be reached in the range $1.5 \leqslant r/D \leqslant 2$, corresponding to the region where the mean heat transfer locally increases. The PDF of the wall shear stress indicates that near-wall backward fluid motions are the most probable in this radial range while being connected with the formation of the secondary vortices. Furthermore, the probability to obtain a very high Nusselt number ($Nu > 100$) is maximum for $r/D = 2$, precisely where the mean Nusselt number exhibits a secondary maximum. The PDF of the Nusselt number is highly skewed in this zone with an exponential tail for the highest values, indicating that the events associated with strong heat transfer are highly intermittent in time and space.

In the range $1.5 \leqslant r/D \leqslant 2$, the PDF of the Nusselt number can be decomposed into two parts. One part is symmetric with respect to the PDF's maximum and corresponds to mild events that lead to a constant mean heat transfer in the range $1.5 \leqslant r/D \leqslant 2$. The residual second part, highly skewed, corresponds to strong events that are responsible for the secondary peak in the radial evolution of the Nusselt number. This PDF analysis suggests that the mild events are connected with the passing of the mainly toroidal large-scale structures, whereas the strong events are related to the azimuthal distortion of these structures and to the simultaneous development of radial vortices that produce the cold spots shown by instantaneous visualisation.

The conditional averaging of the temperature and velocity fields has confirmed that the present phenomenological scenario is statistically representative of the flow in the vicinity of a cold spot. The conditional temperature and velocity fields clearly exhibit a cold fluid flux issuing from the surrounding flow and directed towards the wall by the induced velocity of the secondary vortex. A backward fluid motion is indeed clearly visible at the location of the cold spot. Finally, the conditionally averaged cold spot topology confirms its intermittent character in the azimuthal direction, which strongly breaks the axisymmetry of heat transfer processes.

Acknowledgements

This work was granted access to the HPC resources of IDRIS/CCRT-TGCC under the allocations 2011/12/13/14-020912 made by GENCI (Grand Equipement National de Calcul Intensif). The authors would like to thank S. Roux for many fruitful discussions. The authors are also grateful to E. Dorignac, M. Fénot and G. Lalizel for their help regarding the experimental validation of the present DNS. Finally, the authors are grateful to S. Jordan for his careful proofreading of the present manuscript and to A. Normand for her smart suggestions.

REFERENCES

Ashforth-Frost, S., Jambunathan, K. & Whitney, C. F. 1997 Velocity and turbulence characteristics of a semiconfined orthogonally impinging slot jet. *Exp. Therm. Fluid Sci.* **14** (1), 60–67.

Baughn, J. W. & Shimizu, S. 1989 Heat transfer measurements from a surface with uniform heat flux and an impinging jet. *Trans. ASME J. Heat Transfer* **111**, 1096–1098.

Beaubert, F. & Viazzo, S. 2003 Large eddy simulations of plane turbulent impinging jets at moderate Reynolds numbers. *Intl J. Heat Fluid Flow* **24** (4), 512–519.

Blackwelder, R. F. & Kaplan, R. E. 1976 On the wall structure of the turbulent boundary layer. *J. Fluid Mech.* **76** (1), 89–112.

Buchlin, J. M. 2011 Convective heat transfer in impinging-gas-jet arrangements. *J. Appl. Fluid Mech.* **4** (2), 137–149.

Chung, Y. M. & Luo, K. H. 2002 Unsteady heat transfer analysis of an impinging jet. *Trans. ASME J. Heat Transfer* **124** (6), 1039–1048.

Chung, Y. M., Luo, K. H. & Sandham, N. D. 2002 Numerical study of momentum and heat transfer in unsteady impinging jets. *Intl J. Heat Fluid Flow* **23** (5), 592–600.

Cooper, D., Jackson, D. C., Launder, B. E. & Liao, G. X. 1993 Impinging jet studies for turbulence model assessment – I. Flow-field experiments. *Intl J. Heat Mass Transfer* **36** (10), 2675–2684.

Dailey, G. M. 2000 Design and calculation issues. In *Aero-Thermal Performance of Internal Cooling Systems in Turbomachines*, VKI for Fluid Dynamics Lecture Series, vol. 3, pp. A1–A70.

Dairay, T., Fortuné, V., Lamballais, E. & Brizzi, L. E. 2014 LES of a turbulent jet impinging on a heated wall using high-order numerical schemes. *Intl J. Heat Fluid Flow* **50**, 177–187.

Deshpande, M. D. & Vaishnav, R. N. 1982 Submerged laminar jet impingement on a plane. *J. Fluid Mech.* **114**, 213–226.

Dewan, A., Dutta, R. & Srinivasan, B. 2012 Recent trends in computation of turbulent jet impingement heat transfer. *Heat Transfer Engng* **33** (4–5), 447–460.

Didden, N. & Ho, C.-M. 1985 Unsteady separation in a boundary layer produced by an impinging jet. *J. Fluid Mech.* **160**, 235–256.

Dubief, Y. & Delcayre, F. 2000 On coherent-vortex identification in turbulence. *J. Turbul.* **1**, 1–22.

El Hassan, M., Assoum, H. H., Sobolik, V., Vétel, J., Abed-Meraim, K., Garon, A. & Sakout, A. 2012 Experimental investigation of the wall shear stress and the vortex dynamics in a circular impinging jet. *Exp. Fluids* **52** (6), 1475–1489.

Gardon, R. & Akfirat, J. C. 1965 The role of turbulence in determining the heat-transfer characteristics of impinging jets. *Intl J. Heat Mass Transfer* **8** (10), 1261–1272.

Gauntner, J. W., Livingood, J. N. B. & Hrycak, P. 1970 Survey of literature on flow characteristics of a single turbulent jet impinging on a flat plate. *NASA Tech. Rep.* TN D-5652 NTIS N70-18963.

Hadziabdic, M. & Hanjalic, K. 2008 Vortical structures and heat transfer in a round impinging jet. *J. Fluid Mech.* **596**, 221–260.

Hall, J. W. & Ewing, D. 2006 On the dynamics of the large-scale structures in round impinging jets. *J. Fluid Mech.* **555**, 439–458.

Hunt, J. C. R., Wray, A. A. & Moin, P. 1988 Eddies, stream and convergence zones in turbulent flows. Report CTR-S88, Center For Turbulence Research.

Jambunathan, K., Lai, R., Moss, A. & Button, B. L. 1992 A review of heat transfer data for single circular jet impingement. *Intl J. Heat Fluid Flow* **13**, 106–115.

Kim, J. 1985 Turbulence structures associated with the bursting event. *Phys. Fluids* **28**, 52–58.

Kravchenko, A. G. & Moin, P. 1997 On the effect of numerical errors in large eddy simulation of turbulent flows. *J. Comput. Phys.* **131**, 310–322.

Laizet, S. & Lamballais, E. 2009 High-order compact schemes for incompressible flows: a simple and efficient method with quasi-spectral accuracy. *J. Comput. Phys.* **228**, 5989–6015.

Laizet, S., Lamballais, E. & Vassilicos, J. C. 2010 A numerical strategy to combine high-order schemes, complex geometry and parallel computing for high resolution DNS of fractal generated turbulence. *Comput. Fluids* **39** (3), 471–484.

LAIZET, S. & LI, N. 2011 Incompact3d: a powerful tool to tackle turbulence problems with up to $O(10^5)$ computational cores. *Intl J. Numer. Meth. Fluids* **67** (11), 1735–1757.

LAMBALLAIS, E., FORTUNÉ, V. & LAIZET, S. 2011 Straightforward high-order numerical dissipation via the viscous term for direct and large eddy simulation. *J. Comput. Phys.* **230**, 3270–3275.

LEE, J. & LEE, S.-J. 1999 Stagnation region heat transfer of a turbulent axisymmetric jet impingement. *Expl Heat Transfer* **12** (2), 137–156.

LELE, S. K. 1992 Compact finite difference schemes with spectral-like resolution. *J. Comput. Phys.* **103**, 16–42.

LESIEUR, M., MÉTAIS, O. & COMTE, P. 2005 *Large-Eddy Simulation of Turbulence*. Cambridge University Press.

LODATO, G., VERVISCH, L. & DOMINGO, P. 2009 A compressible wall-adapting similarity mixed model for large-eddy simulation of the impinging round jet. *Phys. Fluids* **21** (3), 035102.

LYTLE, D. & WEBB, B. W. 1994 Air jet impingement heat transfer at low nozzle–plate spacings. *Intl J. Heat Mass Transfer* **37**, 1687–1697.

MANCEAU, R., CARPY, S. & ALFANO, D. 2002 A rescaled $\overline{v^2}f$ model: first application to separated and impinging flows. *Engng Turbul. Modelling Exp.* **5**, 107–116.

MARTIN, H. 1977 Heat and mass transfer between impinging gas jets and solid surfaces. *Adv. Heat Transfer* **13**, 1–60.

MILLER, P. 1995 A study of wall jets resulting from single and multiple inclined jet impingement. *Aeronaut. J.* **99** (986), 201–216.

MOIN, P. & MAHESH, K. 1998 Direct numerical simulation: a tool in turbulence research. *Annu. Rev. Fluid Mech.* **30**, 539–578.

NARAYANAN, V. & PATIL, V. A. 2007 Oscillatory thermal structures induced by unconfined slot jet impingement. *Exp. Therm. Fluid Sci.* **32** (2), 682–695.

NORDSTROM, J., NORDIN, N. & HENNINGSON, D. S. 1999 The fringe region technique and the Fourier method used in the direct numerical simulation of spatially evolving viscous flows. *SIAM J. Sci. Comput.* **20** (4), 1365–1393.

OBOT, N. T., DOUGLAS, W. J. M. & MUJUMDAR, A. S. 1982 Effect of semi-confinement on impingement heat transfer. In *Proceedings of 7th International Heat Transfer Conference*, vol. 3, pp. 395–400.

O'DONOVAN, T. S. & MURRAY, D. B. 2007 Jet impingement heat transfer – part II: a temporal investigation of heat transfer and local fluid velocities. *Intl J. Heat Mass Transfer* **50**, 3302–3314.

ORLANDI, P. & VERZICCO, R. 1993 Vortex rings impinging on walls: axisymmetric and three-dimensional simulations. *J. Fluid Mech.* **256**, 615–646.

POPIEL, C. O. & TRASS, O. 1991 Visualization of a free and impinging round jet. *Exp. Therm. Fluid Sci.* **4**, 253–264.

ROHLFS, W., HAUSTEIN, H. D., GARBRECHT, O. & KNEER, R. 2012 Insights into the local heat transfer of a submerged impinging jet: influence of local flow acceleration and vortex–wall interaction. *Intl J. Heat Mass Transfer* **55** (25), 7728–7736.

ROUX, S., FÉNOT, M., LALIZEL, G., BRIZZI, L.-E. & DORIGNAC, E. 2011 Experimental investigation of the flow and heat transfer of an impinging jet under acoustic excitation. *Intl J. Heat Mass Transfer* **54** (15), 3277–3290.

ROUX, S., FÉNOT, M., LALIZEL, G., BRIZZI, L.-E. & DORIGNAC, E. 2014 Evidence of flow vortex signatures on wall fluctuating temperature using unsteady infrared thermography for an acoustically forced impinging jet. *Intl J. Heat Fluid Flow* **50**, 38–50.

SAGAUT, P. 2005 *Large Eddy Simulation of Incompressible Flow: An Introduction*, 2nd edn. Springer.

SWEARINGEN, J. D., CROUCH, J. D. & HANDLER, R. A. 1995 Dynamics and stability of a vortex ring impacting a solid boundary. *J. Fluid Mech.* **297**, 1–28.

TSUBOKURA, M., KOBAYASHI, T., TANIGUSHI, N. & JONES, W. P. 2003 A numerical study on the eddy structures of impinging jet excited at the inlet. *Intl J. Heat Fluid Flow* **24**, 500–511.

UDDIN, N., NEUMANN, S.-O. & WEIGAND, B. 2013 LES simulations of an impinging jet: on the origin of the second peak in the Nusselt number distribution. *Intl J. Heat Mass Transfer* **57** (1), 356–368.

VEJRAZKA, J., TIHON, J., MARTY, P. & SOBOLIK, V. 2005 Effect of an external excitation on the flow structure in a circular impinging jet. *Phys. Fluids* **17**, 1–14.

VIOLATO, D., IANIRO, A., CARDONE, G. & SCARANO, F. 2012 Three-dimensional vortex dynamics and convective heat transfer in circular and chevron impinging jets. *Intl J. Heat Fluid Flow* **37**, 22–36.

VISKANTA, R. 1993 Heat transfer to impinging isothermal gas and flame jets. *Exp. Therm. Fluid Sci.* **6** (2), 111–134.

WALKER, J. D. A., SMITH, C. R., CERRA, A. W. & DOLIGALSKI, T. L. 1987 The impact of a vortex ring on a wall. *J. Fluid Mech.* **181**, 99–140.

WEBB, B. W. & MA, C.-F. 1995 Single-phase liquid jet impingement heat transfer. *Adv. Heat Transfer* **26**, 105–217.

WILKE, R. & SESTERHENN, J. 2015 Direct numerical simulation of heat transfer of a round subsonic impinging jet. In *Active Flow and Combustion Control 2014*, pp. 147–159. Springer.

YEH, F. C. & STEPKA, F. S. 1984 Review and status of heat-transfer technology for internal passages of air-cooled turbine blades. *NASA Tech. Rep.* 2232.